ACS NANO

www.acsnano.org

Clinically Translatable Injectable Hydrogel Platform for Dual Intraoperative Elevation and Postoperative Healing in Endoscopic Submucosal Dissection

Mengdan Xu,[‖] Wei Peng,[‖] Guangqiu Yu,[‖] Zixuan Xiao, Zhongsheng Zhao, Zelong Xu, Qiankun Shao, Xiuqi Hu, Zeyuan Cao, Mengyao Wu, Xiao Xiao, Yadan Shi, Yongyou Wu,* Jianfeng Zeng,* and Mingyuan Gao*

Cite This: *ACS Nano* 2025, 19, 42331−42348

Read Online

ACCESS | Metrics & More | Article Recommendations | Supporting Information

ABSTRACT: Endoscopic submucosal dissection (ESD) enables en bloc resection of early gastrointestinal neoplasms but remains constrained by two critical limitations: rapid dissipation of submucosal injectates during surgery and insufficient wound management postresection. To overcome this clinical bottleneck, we develop a multifunctional, clinically translatable injectable hydrogel engineered to unify intraoperative mucosal elevation and postoperative tissue repair. This hydrogel system is synthesized via dynamic cross-linking between oxidized sodium alginate and carboxymethyl chitosan, reinforced with Ca^{2+} coordination to enhance mechanical strength and hemostasis. Phycocyanin, a natural antioxidant protein, is incorporated to provide intraoperative visual contrast and bioactive immunomodulatory properties. The formulation exhibits tunable gelation kinetics, excellent injectability, and self-healing capability compatible with endoscopic delivery. Comprehensive in vitro studies confirm the hydrogel's biocompatibility, antioxidant and anti-inflammatory activity, macrophage M2 polarization, hemostatic performance, and structural self-repair. In ex vivo porcine stomach models, the hydrogel achieves sustained mucosal elevation, significantly outperforming hyaluronic acid−based controls. In large-animal ESD models, it promotes organized collagen deposition, angiogenesis, re-epithelialization, and suppressed fibrotic α-SMA expression, collectively accelerating mucosal regeneration with reduced inflammation. This dual-function platform bridges surgical precision with postresection regeneration, offering a next-generation therapeutic material for minimally invasive gastrointestinal oncology.

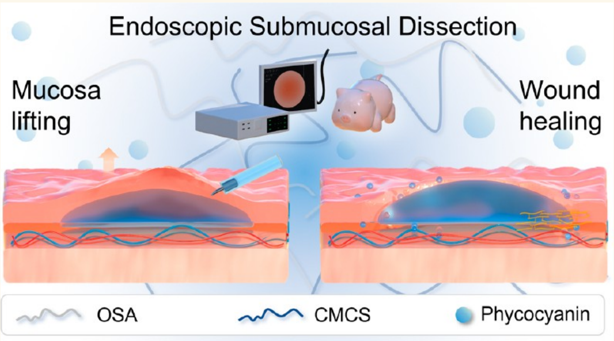

KEYWORDS: *endoscopic submucosal dissection, injectable hydrogel, phycocyanin, wound healing, submucosal injection*

1. INTRODUCTION

Endoscopic submucosal dissection (ESD) is a widely adopted, minimally invasive technique for the en bloc resection of early stage gastrointestinal (GI) neoplasms, including those in the esophagus, stomach, and colon.[1] By enabling precise removal of mucosal and submucosal lesions, ESD avoids radical organ resection and preserves patient quality of life.[2] However, the success of ESD hinges on a technically critical step: the injection of submucosal fluids to create a separation cushion between the mucosal layer and muscularis propria, facilitating safe dissection and minimizing complications such as bleeding and perforation.[3,4]

Current clinical injectates such as normal saline,[5] glycerol,[6] and sodium hyaluronate[7] present clear limitations. Their low viscosity and poor tissue retention lead to rapid diffusion after injection, requiring repeated reinjections to maintain mucosal elevation.[8] This not only prolongs surgical time but also

Received: August 18, 2025
Revised: November 25, 2025
Accepted: November 26, 2025
Published: December 5, 2025

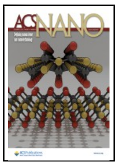

Scheme 1. Schematic Illustration of the Bioactive Hydrogel System and Its Application in Endoscopic Submucosal Dissection (ESD). (a) The Injectable Hydrogel System is Formed by Mixing Two Precursor Solutions: Solution I Contains Oxidized Sodium Alginate (OSA); Solution II Includes Carboxymethyl Chitosan (CMCS), Phycocyanin (PC), and Calcium Ions (Ca^{2+}). Upon Mixing, the Components Undergo Gelation and Are Delivered via Endoscopic Submucosal Injection into the Gastric Submucosal Space Using a Clinical Injection Needle. (b) Molecular-Level Schematic of the Dynamic Hydrogel Network. Schiff Base Reactions between Aldehyde Groups on OSA and Amine Groups on CMCS Form Reversible Covalent Crosslinks, While Ca^{2+} Coordinates with Carboxyl Groups for Secondary Ionic Crosslinking. Phycocyanin is Physically Embedded within the Network and Contributes Antioxidant and Anti-Inflammatory Bioactivity. (c) Illustration of the ESD Procedure: ① Identification of the Lesion by Endoscopic Inspection; ② Submucosal Injection of the Hydrogel to Elevate the Mucosal Layer and Separate It from the Muscularis Propria; ③ Mucosal Dissection Using an Electric Knife; ④ Postoperative Wound Management. The Hydrogel Supports Effective Mucosal Elevation to Facilitate Lesion Resection and Subsequently Modulates the wound Microenvironment by Releasing PC to Reduce Pro-Inflammatory Cytokines (TNF-α, IL-6), Oxidative Stress (ROS, NO), and Actively Induces M2 Macrophage Polarization, Thereby Promoting Accelerated Epithelial Healing

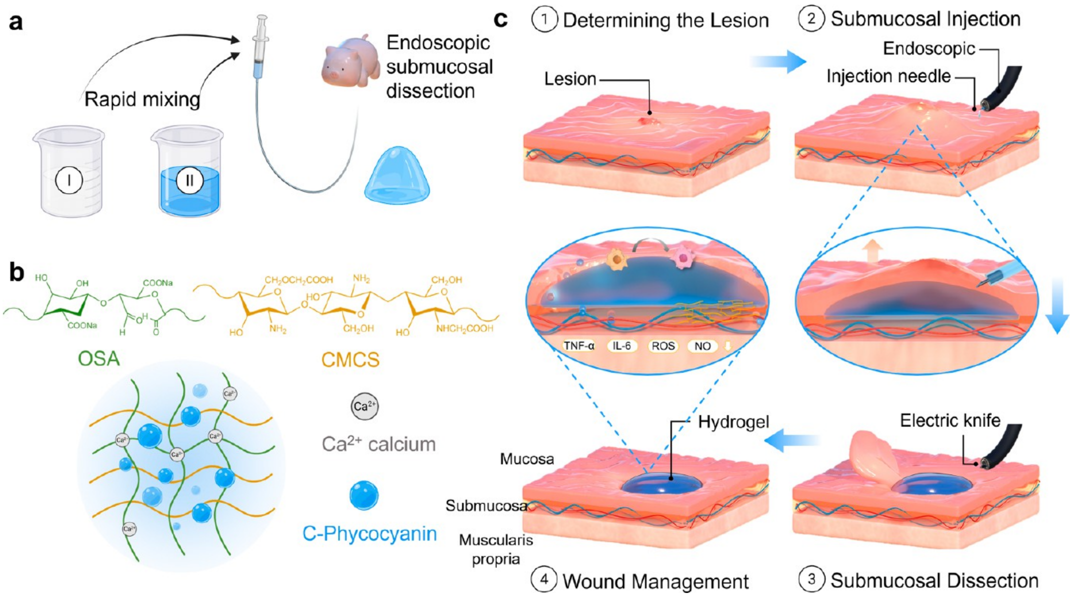

increases the risk of procedural failure and complications.[9] Commercial products such as MucoUp, essentially a sodium hyaluronate solution, or Eleview, a poloxamer-based formulation with enhanced cushion durability, have been adopted to address some of these issues.[10,11] However, despite offering improved performance, their cost and limited biofunctionality remain concerns. More recent agents such as ORISE gel have further raised serious concerns in clinical practice.[12,13] Reports have shown that ORISE may cause submucosal deposition and provoke extensive foreign-body giant cell granulomatous reactions involving the submucosa and muscularis propria, interfering with histopathological interpretation and potentially leading to misdiagnosis or overtreatment.[14,15] Furthermore, these materials typically disperse upon mucosal incision and fail to remain in situ to protect the wound surface postoperatively. These shortcomings underscore the unmet clinical need for next-generation submucosal injectates that not only perform well during surgery but also actively support post-ESD wound healing.

Injectable hydrogels have emerged as attractive candidates for minimally invasive surgery due to their in situ gelation, tissue adhesiveness, and tunable mechanical properties. Although no hydrogel-based formulation has yet received regulatory approval for clinical use in ESD, a growing body of preclinical evidence underscores their potential to outperform conventional solutions. Various natural and synthetic polymers such as alginate,[16−18] gelatin,[19−21] and block copolymers[22] have shown promise in improving mucosal elevation. However, these systems frequently face functional trade-offs. Thermosensitive hydrogels (such as CS-GP,[23,24] HpHCS-PVP-GP,[20] HBC-SA,[25] etc.) may undergo premature gelation within the injection needle due to the uncertainty associated with the temperature change from ambient conditions to body temperature, making the gelation time difficult to control. Shear-thinning hydrogels (such as ISAH,[17] βCP,[26] CMS/Lap,[27] etc.), while easier to inject, exhibit insufficient mechanical stability under physiological stresses such as respiratory motion and gastrointestinal peristalsis.[28,29] Dual-component chemically cross-linked systems offer better stability but can be difficult to inject due to rapid gelation.[30] Despite their structural differences, these formulations provide little support for postoperative healing. To overcome these challenges, recent efforts have turned to biofunctional hydrogels incorporating drugs[31] or nanoparticles[32] for therapeutic benefit. Although such systems demonstrate biological activity, including antimicrobial effects and the promotion of angiogenesis, their multicomponent formulation complexity compromises stability, limits reproducibility, and impedes clinical translation. An ideal solution would be a material that delivers both surgical performance and therapeutic functionality, with a simple, injectable format amenable to clinical use.

In this context, phycocyanin (PC), a blue chromoprotein derived from cyanobacteria, represents a uniquely advantageous bioactive component.[33] PC possesses potent anti-inflammatory[34] and antioxidant[35] properties and has been

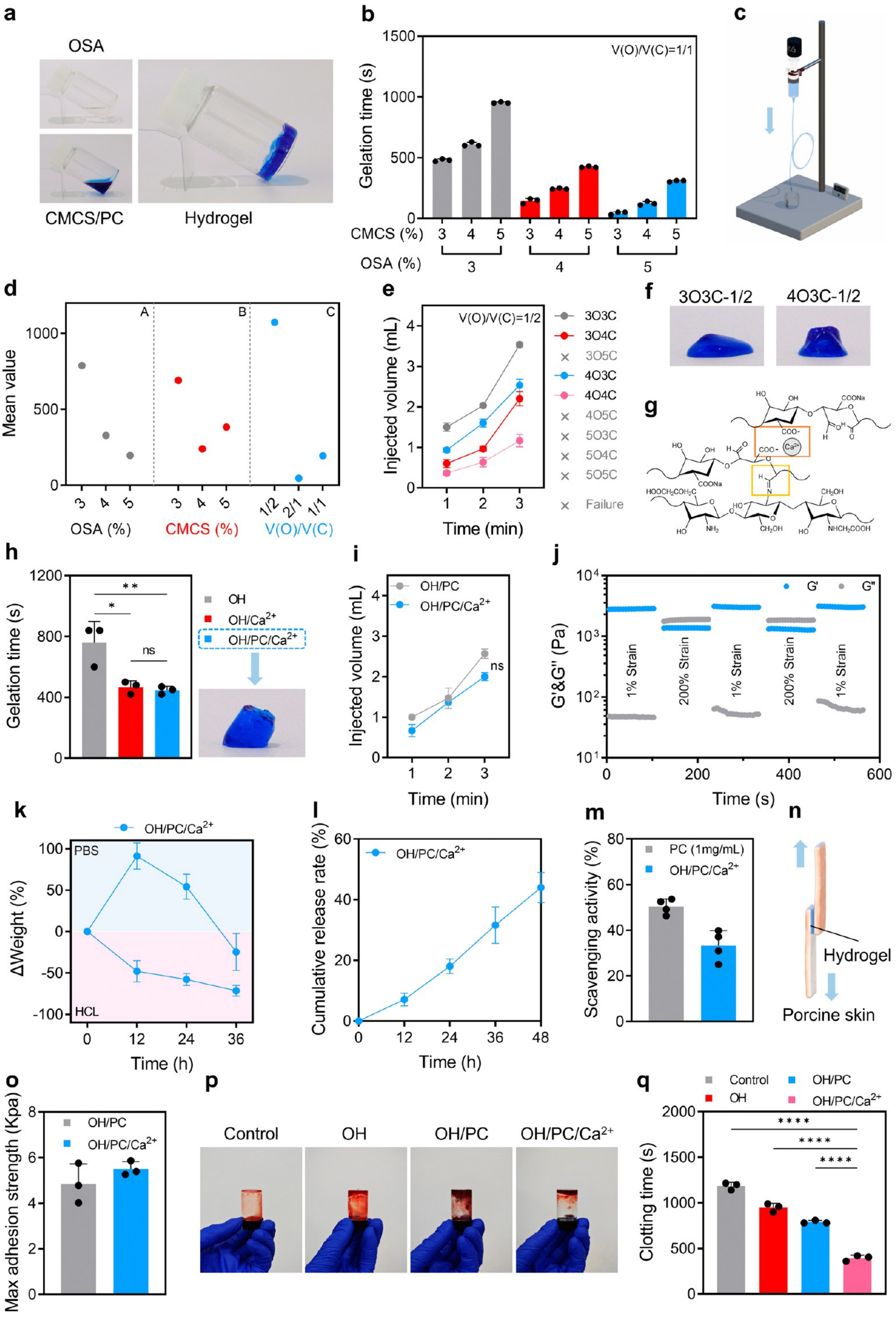

Figure 1. Optimization and characterization of a multifunctional bioactive hydrogel for submucosal injection in endoscopic submucosal dissection (ESD). (a) Representative images showing in situ gelation of the hydrogel upon mixing sodium alginate (OSA) solution with a phycocyanin (PC)-containing carboxymethyl chitosan (CMCS) solution. (b) Gelation times of xOyC-1/1 hydrogels (*x*, *y* = 3−5 wt %) at a

Figure 1. continued

fixed OSA:CMCS volume ratio of 1:1 (V(O)/V(C) = 1/1) ($n = 3$). (c) Custom-built apparatus simulating manual injection through fine-gauge endoscopic needles. (d) Mean effect values from orthogonal design analysis evaluating the influence of three parameters: OSA concentration (Factor A), CMCS concentration (Factor B), and volume ratio V(O)/V(C) (Factor C) on gelation time. (e) Injected volumes of xOyC-1/2 hydrogels through the device within 3 min ($n = 3$). (f) Macroscopic images of 3O3C-1/2 and 4O3C-1/2 formulations after gelation. (g) Schematic diagram illustrating the dual-cross-linked hydrogel network formed by dynamic Schiff base bonding and Ca^{2+} ionic coordination. (h) Gelation times of optimized hydrogels with and without PC and Ca^{2+} ($n = 3$). (i) Injectability of OH/PC and OH/PC/Ca^{2+} formulations over time ($n = 3$). (j) Rheological performance of OH/PC/Ca^{2+} hydrogel under alternating strain conditions demonstrating self-healing capability. (k) Mass loss profiles of OH/Ca^{2+} and OH/PC/Ca^{2+} hydrogels incubated in PBS or dilute HCl (pH 2.4) for up to 36 h ($n = 3$). (l) Cumulative PC release from OH/PC/Ca^{2+} hydrogels in PBS over 48 h ($n = 3$). (m) DPPH-based radical scavenging activity of free PC (1 mg/mL) and OH/PC/Ca^{2+} hydrogel ($n = 4$). (n) Schematic of lap shear adhesion test on porcine skin. (o) Maximum tissue adhesive strength of OH/PC and OH/PC/Ca^{2+} measured on porcine skin ($n = 3$). (p) Photographs showing clot formation in inverted-tube assays with control blood and blood treated with OH, OH/PC, or OH/PC/Ca^{2+} hydrogels. (q) Quantification of clotting times under each treatment condition ($n = 3$). Statistical significance: ns = not significant, $^{*}p < 0.05$, $^{**}p < 0.01$, $^{***}p < 0.001$, $^{****}p < 0.0001$.

shown to promote macrophage M2 polarization, scavenge reactive oxygen species (ROS), and modulate cytokine production as demonstrated in gastric ulcers,[36] intestinal inflammation,[37] wound healing,[38,39] radiation-induced injury,[40] and pulmonary fibrosis.[41] These functions contribute to an immunomodulatory and pro-regenerative wound microenvironment. Moreover, PC's vivid blue coloration enables real-time visualization of the injectate under endoscopic guidance, providing a nontoxic alternative to methylene blue,[42] which has raised safety concerns including DNA damage.[43]

In this study, we developed a clinically translatable injectable hydrogel platform comprising oxidized sodium alginate (OSA) and carboxymethyl chitosan (CMCS), dynamically cross-linked via Schiff base chemistry and structurally reinforced with calcium ions (Ca^{2+}). This system was designed to address both intraoperative and postoperative needs in ESD: enabling durable mucosal elevation, effective hemostasis, precise delivery through fine-gauge needles, and sustained PC-mediated bioactivity. We systematically evaluated the hydrogel's physicochemical properties, including gelation kinetics, mechanical strength, self-healing, and degradation behavior. Its bioactivity was assessed through in vitro assays for cytocompatibility, ROS scavenging, and immunomodulation. Ex vivo porcine stomach models were used to test mucosal elevation and tissue retention. Finally, we employed a large-animal porcine ESD model to assess the hydrogel's therapeutic potential, focusing on key histological parameters including inflammation resolution, collagen remodeling, angiogenesis, and epithelial regeneration. Through this integrated strategy, we aim to establish a next-generation, biofunctional submucosal injection platform that addresses long-standing limitations in ESD, bridging intraoperative procedural needs with biologically guided mucosal healing to support clinical translation (Scheme 1).

2. RESULTS AND DISCUSSION

2.1. Design and Characterization of Injectable Hydrogels for ESD.

As a foundational polymer, OSA was synthesized via selective oxidation using sodium periodate.[44] This reaction targets vicinal hydroxyl groups at the C2 and C3 positions of the alginate backbone, generating dialdehyde functionalities that serve as reactive cross-linking sites. The degree of oxidation was determined to be 43.2% via hydroxylamine hydrochloride titration, and the successful introduction of aldehyde groups was confirmed by the emergence of a characteristic infrared absorption band at 1722 cm^{-1} (Figure S1). These aldehyde groups enable Schiff base formation with primary amines, offering dynamic and reversible covalent cross-linking chemistry suited for injectable, self-healing systems.

To construct a hydrogel matrix, the OSA solution was mixed with a CMCS solution containing PC (Figure 1a). CMCS was selected as the amino-functionalized counterpart due to its biocompatibility,[45] mild gelation behavior,[46] and known hemostatic properties.[47] The hydrogel cross-linking was driven by imine formation between the aldehyde groups of OSA and the primary amines on CMCS. In parallel, hydrogen bonding between PC and CMCS further contributed to network stability.[48] PC, a chromoprotein derived from cyanobacteria, was included not only for its potent anti-inflammatory and antioxidant functions but also for its intense blue coloration, which facilitates intraoperative visualization under endoscopic guidance.[33] Together, these interactions yielded a dynamically cross-linked, visibly traceable, and potentially bioactive hydrogel.

Given the structural design, we next focused on optimizing injectability, arguably the most clinically critical parameter for real-world application. Endoscopic injectates must be delivered through specialized needles that are approximately 2 m long with internal diameters less than 2 mm (Figure S2), meaning that formulations must remain flowable under moderate manual pressure yet quickly gel upon reaching the tissue site. To characterize this window, we prepared a series of hydrogel precursor mixtures with varying concentrations of OSA (3–5%, w/v) and CMCS (3–5%, w/v), maintaining a constant volume ratio V(O)/V(C) of 1:1. We denoted each formulation using the shorthand *x*O*y*C-*z*, where *x* and *y* indicate the percentage weight of OSA and CMCS, and *z* represents the volume ratio.

We first assessed gelation kinetics using a magnetic stirring–assisted inversion method (Figure S3). Increasing the CMCS concentration from 3% to 5% delayed gelation significantly, due to elevated solution viscosity impeding mass transport and slowing imine bond formation (Figure 1b). In contrast, increasing OSA content accelerated gelation by increasing the density of aldehyde groups, thereby promoting cross-link density. These opposing trends highlight the need to balance reactive group availability with solution fluidity to maintain suitable working times.

However, gelation time alone does not guarantee clinical usability. To evaluate realistic delivery performance, we constructed a vertical injection apparatus to simulate hand-push injection through fine-gauge tubing (Figure 1c). Testing across nine *x*O*y*C-1/1 formulations revealed that none achieved an injection volume >0.5 mL within 3 min (Figure S4), indicating poor deliverability. This prompted us to perform an orthogonal experimental optimization to explore three primary variables—OSA concentration (Factor A), CMCS concentration (Factor B), and volume ratio (Factor C)—on gelation time (Table S1). Range Analysis showed that volume ratio (V(O)/V(C)) exerted the dominant influence on gelation times (RC > RA > RB), where R (range) quantifies the effect magnitude of factor levels on the response variable in orthogonal experimental design. The V(O)/V(C) = 2:1 ratio induced gelation times under 1 min, too rapid for clinical manipulation, while 1:2 significantly prolonged the workable window (Figure 1d).

Among the formulations tested under the V(O)/V(C) = 1/2 ratio, four candidates (3O3C-1/2, 3O4C-1/2, 4O3C-1/2, and 4O4C-1/2) demonstrated sufficient flowability with injection volumes exceeding 1 mL within 3 min (Figure 1e). Although the 3O3C-1/2 formulation demonstrates good injectability, it exists in a weak gel state, with a gelation time exceeding 30 min. Notably, the 4O3C-1/2 formulation exhibited an optimal balance between injectability, moderate gelation time, and stable postinjection structural integrity (Figure 1f), and was thus selected as the optimized hydrogel (hereafter designated OH). This formulation became the foundational matrix for all subsequent modifications and analyses.

To further enhance mechanical robustness while maintaining biocompatibility, we introduced a secondary cross-linking network by incorporating calcium ions (Ca^{2+}). This strategy is well-documented in alginate chemistry, where divalent cations chelate with carboxylate groups to establish additional ionic cross-links.[49] In our system, Ca^{2+} ions were introduced at 0.009 M final concentration, which rapidly interacted with OSA chains to form a stiffer hydrogel matrix (Figure 1g). The addition of Ca^{2+} accelerated gelation by approximately 38.6% (Figure 1h), further tightening the dynamic network without adversely affecting injectability (Figure 1i). FTIR analysis corroborated these chemical transitions, with strong imine peak formation (C═N stretch at 1600 cm^{-1}) and characteristic COO^- coordination shifts (Figure S5), validating the dual-network architecture. Scanning electron microscopy revealed that the Ca^{2+}-reinforced hydrogel (OH/PC/Ca^{2+}) exhibited a more compact, uniformly distributed porous microstructure compared to the singly cross-linked version (Figure S6), suggesting improved internal cohesion and load distribution.

Given the mechanical challenges posed by gastrointestinal motility, we next examined the hydrogel's self-healing capability, which is essential for maintaining barrier function under stress. Macroscopic tests showed that two severed hydrogel segments, one colored with PC and one uncolored, could autonomously fuse after a period of rest without external triggers. Moreover, when fragmented gel pieces are reassembled in a mold, the breakage and subsequent reconnection of their dynamic bonds enable the gel to support its own weight during handling (Figure S7). These observations were mechanistically validated by oscillatory rheology: under 200% strain, G' dropped significantly, indicating partial network disruption; however, upon returning to 1% strain, G' recovered fully (Figure 1j). This dynamic reversibility arises from the cooperative interplay of three reversible interactions in the hybrid network: primary covalent imine (Schiff base) bonds, secondary ionic coordination via Ca^{2+} chelation, and auxiliary hydrogen bonding.

We further evaluated the hydrogel's environmental stability and degradation kinetics under simulated physiological and gastric conditions. In phosphate-buffered saline (PBS), OH/PC/Ca^{2+} reached swelling equilibrium within 12 h, with a final swelling ratio of 91.3%. Subsequently, its mass decreased below the initial value after 36 h and underwent complete disintegration within 5 days. Under acidic conditions (pH = 2.4), simulating the stomach microenvironment, degradation proceeded more rapidly: OH/PC/Ca^{2+} lost ~71.4% of its mass within 36 h (Figure 1k). These results confirm that the hydrogel exhibits degradation behavior, which may be favorable for timely clearance following wound healing.

The hydrogel was also evaluated for its potential as a localized drug reservoir. We quantified phycocyanin (PC) release over 48 h in PBS, observing a sustained release profile with ~44.0% cumulative release (Figures 1l, S8). Given PC's known antioxidant properties, we conducted DPPH free radical scavenging assays. Free PC (1 mg/mL) exhibited a radical scavenging activity of 50.2%, while the hydrogel-encapsulated PC retained 30.9% activity (Figure 1m). The observed retention may be due to the protection of PC within the hydrogel matrix and its controlled release into the surrounding environment, ensuring both stability and bio-functionality over the critical early postinjection period.

To confirm that the hydrogel could remain adherent to wet, dynamically stressed tissues, we performed ex vivo adhesion tests on porcine gastric and dermal surfaces. After simulated mechanical deformation (bending and extrusion), OH/PC/Ca^{2+} remained strongly adhered to the tissue surface (Figure S9). Lap shear tests quantified this effect, yielding a maximum adhesion strength of 5.5 ± 0.3 kPa comparable to that of commercial medical adhesives such as skin plasters (Figures 1n,o and S10). This characteristic demonstrates that the hydrogel can be retained at the surgical site postoperatively for extended periods, functioning as a physical barrier while enabling sustained drug release to facilitate wound healing.

Lastly, we investigated the hydrogel's capacity to promote hemostasis, an essential function during and after ESD. Chitosan has intrinsic platelet-aggregating properties[50] and Ca^{2+} serves as a cofactor in the coagulation cascade.[51] In vitro clotting assays demonstrated that while untreated activated whole blood clotted in ~1185 s, addition of OH/PC/Ca^{2+} significantly shortened this to ~395 s (Figure 1p,q). This enhancement of coagulation performance underscores the hydrogel's potential to serve not only as an elevation agent but also as a hemostatic wound sealant during ESD procedures.

2.2. Evaluation of Dye Diffusion, Mucosal Elevation Capacity, and Biocompatibility of OH/PC/Ca^{2+} Hydrogel.

A hallmark feature of PC is its intrinsic vivid blue pigmentation, which enables its dual role as a bioactive agent and a visual contrast enhancer during endoscopic procedures. In conventional ESD, methylene blue (MB) is frequently used to delineate lesions intraoperatively.[42] However, MB suffers from several notable drawbacks: its low molecular weight (~320 Da) facilitates rapid and uncontrolled diffusion in tissue or fluid environments, leading to uneven staining, visual oversaturation, and poor field demarcation that increase procedural complexity and risk.

To evaluate whether PC-based hydrogels could improve contrast localization and mitigate dye dispersion, we developed an in vitro dye diffusion model using PBS as the release medium. Three test conditions were compared: (i) a clinically accepted HA/MB solution (0.4% hyaluronic acid and 0.07%

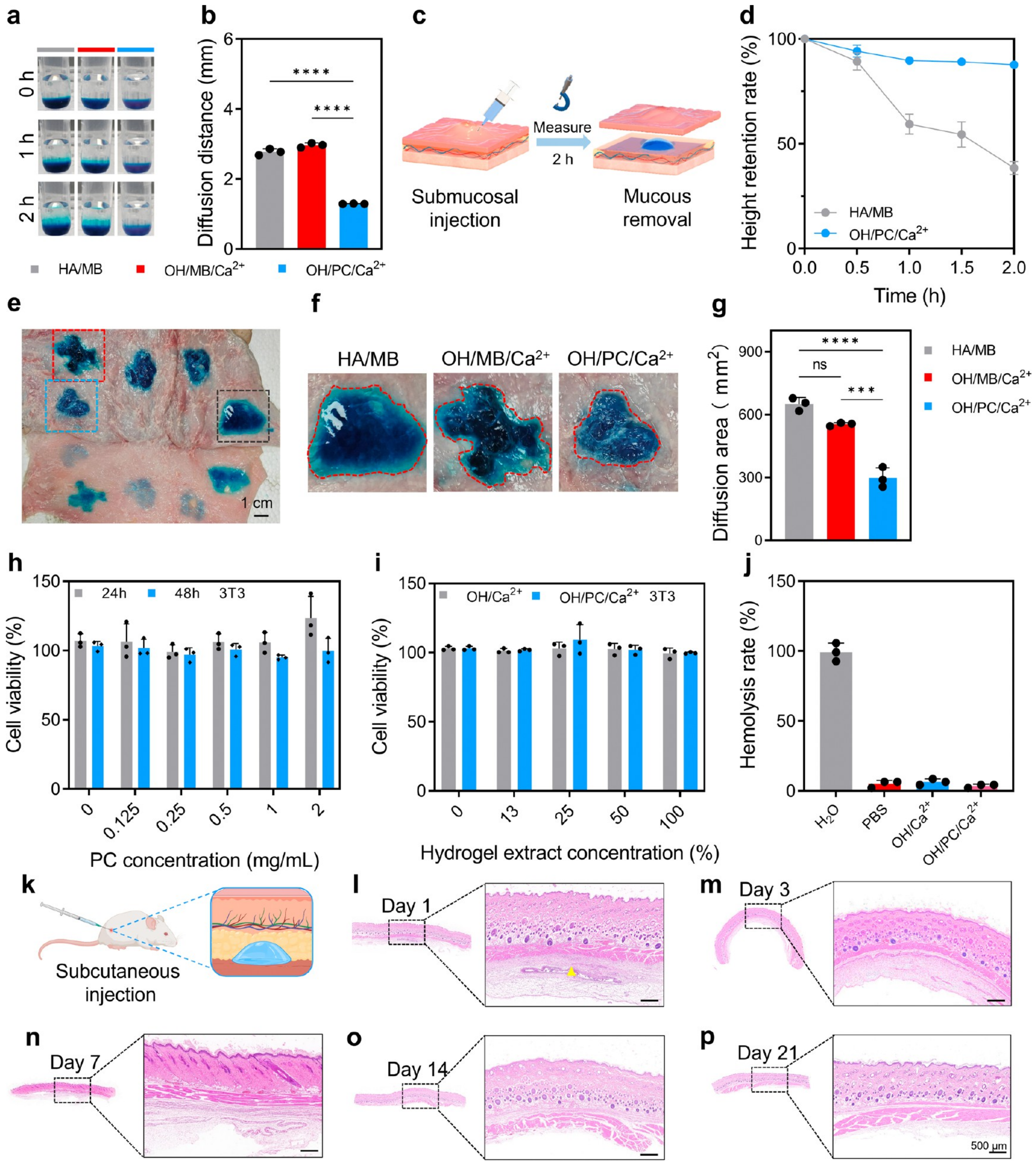

Figure 2. Evaluation of dye diffusion, mucosal elevation capacity, and biocompatibility of OH/PC/Ca^{2+}hydrogel. (a) Diffusion images of methylene blue (MB) and phycocyanin (PC) from HA/MB, OH/MB/Ca^{2+}, and OH/PC/Ca^{2+} formulations in PBS over time. (b) Quantitative measurement of dye diffusion distance ($n = 3$). (c) Schematic of ex vivo porcine gastric submucosal injection and measurement of mucosal elevation height at designated time points. (d) Retention rate of mucosal elevation over 120 min after submucosal injection ($n = 3$). (e) Representative images of submucosal areas after removal of mucosa 2 h postinjection. (f) Visual spread of MB or PC in explanted tissue and (g) quantification of diffusion area ($n = 3$). (h) Cell viability of NIH-3T3 fibroblasts after 24 and 48 h culture with different concentrations of free PC ($n = 3$). (i) Cytocompatibility evaluation of NIH-3T3 fibroblasts cultured for 24 h with extract from OH/Ca^{2+} or OH/PC/Ca^{2+} hydrogels (0.1 g/mL, 48 h preincubation) ($n = 3$). (j) Hemolysis ratio of hydrogel samples using fresh blood; PBS and deionized water served as negative and positive controls, respectively ($n = 3$). (k) Schematic of subcutaneous hydrogel injection in rat dorsal. (l–p) H&E-stained histological sections of skin tissues at day 1, day 3, day 7, day 14, and day 21 postinjection. The triangle indicates the inflammatory response at the gel injection site. Data are presented as mean ± SD. Statistical significance: ns = not significant, *$p < 0.05$, **$p < 0.01$, ***$p < 0.001$, ****$p < 0.0001$.

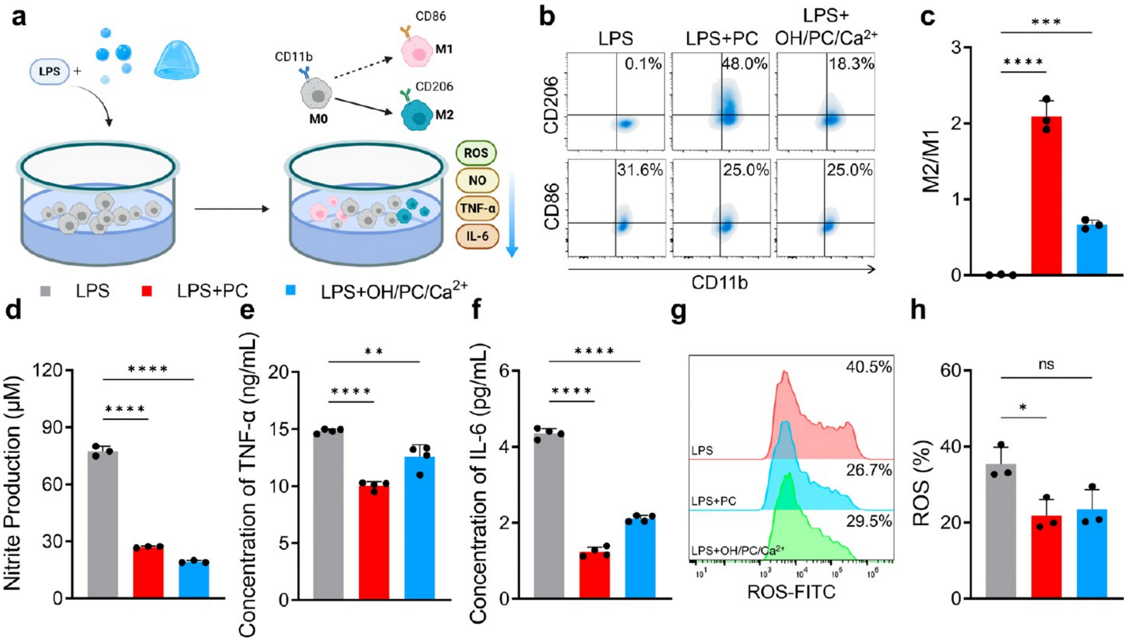

Figure 3. Immunomodulatory and antioxidant effects of PC and OH/PC/Ca^{2+}hydrogel on LPS-stimulated macrophages. (a) Schematic illustrating the enhancement of M2 polarization and reduction of inflammatory cytokines by phycocyanin (PC) and OH/PC/Ca^{2+}hydrogel in macrophages costimulated with Lipopolysaccharide (LPS). (b) Representative flow cytometry plots showing $CD206^+/CD11b^+$ (M2) and $CD86^+/CD11b^+$ (M1) expression in RAW 264.7 macrophages treated with LPS alone, LPS + PC, or LPS + OH/PC/Ca^{2+}. (c) Quantified M2/M1 ratio from flow cytometric analysis ($n = 3$). (d) Nitrite production content in cell culture supernatants determined via Griess assay ($n = 3$). (e,f) ELISA quantification of pro-inflammatory cytokines TNF-*α* and IL-6, respectively ($n = 4$). (g) Intracellular ROS levels assessed by DCFH-DA staining and flow cytometry. (h) Quantification of ROS-positive cells ($n = 3$). Data are presented as mean ± SD. Statistical significance: ns = not significant, $*p < 0.05$, $**p < 0.01$, $***p < 0.001$, $****p < 0.0001$.

MB), (ii) OH/MB/Ca^{2+} hydrogel incorporating 0.07% MB, and (iii) OH/PC/Ca^{2+} hydrogel incorporating 1% PC. As shown in the Figure, MB rapidly diffused in both HA and hydrogel matrices, whereas PC remained largely confined within the OH/PC/Ca^{2+} gel (Figure 2a). Quantitative analysis confirmed significantly lower diffusion distances in the PC group (Figure 2b). This retention is primarily attributed to the high molecular weight of PC (~240 kDa), which—unlike MB—forms hydrogen bonding networks within the hydrogel matrix, thereby reducing its outward migration.

To assess the capacity to sustain mucosal mound elevation, submucosal injections were performed on freshly harvested porcine stomach tissue (Figures 2c, S11). Equal volumes of either HA/MB solution or hydrogel formulations were injected into the submucosa, and the resulting mucosal elevation height was monitored over a 2 h period using a digital micrometer. The HA/MB solution exhibited a steep decline in mucosal elevation: by 30 min, the retained height had dropped to 59.4%, and by 2 h, it fell to 38.5%. In contrast, OH/PC/Ca^{2+} hydrogel maintained a robust mucosal cushion throughout the observation window, retaining 87.7% of its initial height at 2 h (Figure 2d). This sustained lift reflects the superior mechanical stability and in situ persistence of the dual-network hydrogel to meet surgical requirements.

Following the 2 h injection window, mucosal layers were carefully peeled off to expose the submucosal space and visualize dye distribution (Figure 2e). Image analysis revealed that HA/MB and OH/MB/Ca^{2+} exhibited large diffusion areas (650.6 mm^2 and 553.8 mm^2, respectively), indicative of widespread dispersion. By contrast, OH/PC/Ca^{2+} showed significantly reduced spread (298.6 mm^2), corroborating its ability to confine PC within a localized microenvironment (Figure 2f,g). This is a critical attribute for intraoperative navigation, allowing endoscopists to more accurately localize lesions and minimize tissue misidentification.

Given its proposed translational application, the biocompatibility of the OH/PC/Ca^{2+} hydrogel was rigorously evaluated in accordance with ISO 10993 standards. We assessed cytocompatibility, hemocompatibility, and local tissue responses. For cytotoxicity assessment, NIH-3T3 fibroblasts were incubated with varying concentrations of free PC (ranging from 0 to 2 mg/mL) for 24 and 48 h. Across all concentrations and time points, cell viability remained above 95%, with no observable morphological abnormalities (Figure 2h). This confirmed that PC, even at higher doses, does not adversely affect fibroblast proliferation. To further evaluate the material's biosafety, extract-based assays were conducted using hydrogel leachates (0.1 g/mL, preincubated for 48 h). NIH-3T3 cells cultured in hydrogel extracts for 24 h maintained high viability (>95%) for both OH/PC/Ca^{2+} and OH/Ca^{2+} groups, indicating minimal cytotoxic leaching (Figure 2i).

The hemocompatibility of the hydrogels was tested via in vitro hemolysis assays using fresh blood. Compared to water (positive control), which induced pronounced hemolysis, the OH/Ca^{2+} and OH/PC/Ca^{2+} formulations exhibited hemolysis ratios of 6.5% and 3.6%, respectively, comparable to the PBS control of 5.0% (Figures 2j, S12). This suggests that the materials do not disrupt red blood cell membranes, satisfying hemocompatibility criteria for injectable biomaterials.

To further validate in vivo tolerance, the hydrogel was subcutaneously injected into the dorsal skin of Sprague–Dawley rats (Figure 2k). In skin specimens harvested on days 1, 3, 7, 14, and 21 postinjection, discrete blue gel remnants were observed subcutaneously on days 1 and 3, which were

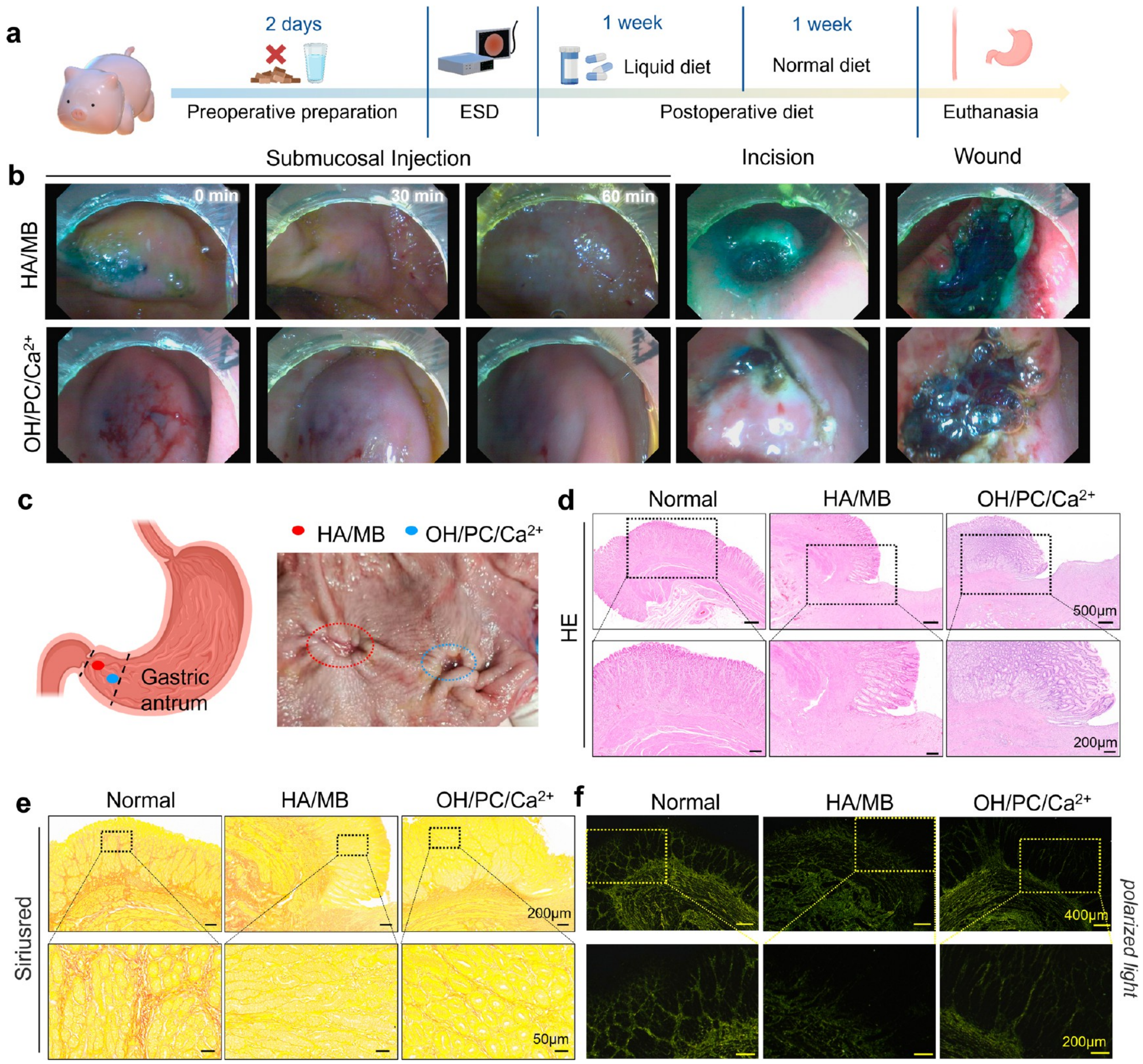

Figure 4. In vivo evaluation of OH/PC/Ca^{2+}hydrogel in a porcine ESD model. (a) Schematic timeline of the porcine ESD procedure and postoperative evaluation. (b) Representative endoscopic images of mucosal elevation at 0, 30, and 60 min following submucosal injection of HA or OH/PC/Ca^{2+} hydrogel, followed by mucosal incision and wound formation. (c) Anatomical illustration of the gastric antrum showing the wound site and gross images of the gastric mucosa 14 days post-ESD, highlighting HA-treated (red circle) and hydrogel-treated (blue circle) regions. (d) H&E-stained histological sections showing wound healing and re-epithelialization at the lesion site. (e) Sirius Red-stained sections under white light indicating collagen deposition; inset shows higher magnification. (f) Polarized light microscopy revealing the birefringent collagen structure, mainly type III collagen fibers. Scale bars as indicated.

completely resolved by day 7. The gel implantation elicited a transient and self-resolving inflammatory response, characterized by localized inflammatory cell infiltration at the injection site on day 1. This initial response underwent complete resolution as the gel degraded, with no histological evidence of inflammation observed from day 7 through the study end point on day 21. The dermal collagen matrix remained structurally intact (Figure 2l−p), supporting the hydrogel's excellent tissue compatibility and biodegradability. Taken together, these results establish that OH/PC/Ca^{2+} hydrogel not only prolongs mucosal elevation and minimizes intraoperative dye dispersion but also exhibits high biocompatibility across cellular, hematological, and tissue-level evaluations, affirming its safety for potential clinical application in ESD.

2.3. Immunomodulatory and Antioxidant Effects of PC and OH/PC/Ca^{2+} Hydrogel in an In Vitro Macrophage Model. Macrophages play an indispensable role throughout the wound healing cascade, engaging in both the clearance of pathogens and orchestration of tissue repair.[52] In response to inflammatory stimuli during the early phase, macrophages adopt the M1 phenotype, characterized by the release of pro-inflammatory cytokines and reactive species. As healing progresses, a phenotypic transition toward the alternatively activated M2 state supports anti-inflammatory signaling, extracellular matrix remodeling, and tissue regeneration. Guiding this M1-to-M2 shift is widely recognized as a therapeutic strategy to accelerate wound resolution.[53] To explore the immunomodulatory potential of PC and PC-loaded hydrogel (OH/PC/Ca^{2+}), an in vitro inflammatory model was established using RAW 264.7 macrophages stimulated with lipopolysaccharide (LPS). Cells were then treated with PC or hydrogel extracts, and phenotypic markers CD86 (M1) and CD206 (M2) were quantified via flow cytometry on $CD11b^+$ gated populations. Notably, PC and OH/PC/Ca^{2+} treatments significantly increased the M2/M1 ratio, with the hydrogel showing a markedly enhanced M2 polarization compared to LPS-alone groups (Figure 3a−c). Although the OH/PC/Ca^{2+} group exhibited slightly lower CD206 expression than the free PC group, this may result from the hydrogel's modulation of PC release kinetics and cellular interactions. Notably, the PC-free hydrogel group (LPS + OH/Ca^{2+}) failed to induce any significant M2 polarization (Figure S13a). Corroborating this phenotypic modulation, the secretion of classical pro-inflammatory mediators was substantially reduced in treated macrophages. Nitric oxide (NO), a hallmark of M1 macrophage activation, was significantly suppressed as measured by the Griess assay (Figure 3d). Additionally, enzyme-linked immunosorbent assays (ELISAs) revealed significantly lower levels of tumor necrosis factor-α (TNF-α) and interleukin-6 (IL-6) in the culture supernatants of hydrogel-treated cells, suggesting potent attenuation of LPS-induced inflammation (Figure 3e,f).

Beyond immunomodulation, phycocyanin is renowned for its intrinsic antioxidant capacity, attributable to its tetrapyrrole chromophore structure.[54] To evaluate intracellular oxidative stress, we quantified ROS using DCFH-DA staining followed by flow cytometry. The flow cytometry results revealed that the ROS-positive cell population was 35.4 ± 4.4% in the LPS-treated group, which was significantly higher than that in the LPS + PC group (21.8 ± 4.2%) and the LPS + OH/PC/Ca^{2+} group (23.5 ± 5.2%). These data indicate that both PC and OH/PC/Ca^{2+} effectively reduced intracellular ROS levels, demonstrating their ROS scavenging capacity (Figure 3g,h). The proportion of ROS-positive macrophages in the LPS + OH/Ca^{2+} group (37.8% ± 4.9%) was not significantly different from that in the LPS group (Figure S13b), suggesting minimal antioxidant effect in the absence of PC. Consistent with the ROS suppression, malondialdehyde (MDA), a key marker of lipid peroxidation and cellular oxidative damage, was significantly decreased in the LPS + OH/Ca^{2+}-treated group (Figure S14).

Mechanistically, the immunomodulatory and antioxidant effects of phycocyanin observed in this study are supported by prior literature implicating several signaling cascades.[40] The anti-inflammatory activity of PC is predominantly mediated through inhibition of the NF-κB pathway. NF-κB is a central regulator of innate immune responses, governing the transcription of pro-inflammatory cytokines such as TNF-α, IL-6, and IL-1β.[55] In LPS-stimulated macrophages, PC has been shown to suppress NF-κB activation, thereby attenuating inflammatory signaling,[56] protecting gastric epithelial tissues,[36] and ameliorating colonic mucosal injury in inflammatory bowel disease models.[57] In parallel, the antioxidant effects of PC are largely attributed to the activation of the Nrf2 pathway, a key transcriptional regulator of cellular redox homeostasis. By promoting Nrf2 nuclear translocation and upregulating its downstream effectors, particularly heme oxygenase-1 (HO-1), PC enhances the cell's capacity to scavenge ROS and mitigate oxidative damage.[58] These pathways are implicated in various oxidative stress-related injuries, including hepatic,[59] dermal,[60] and pancreatic models.[61]

Notably, the encapsulation of PC within the hydrogel matrix may enhance its bioavailability and temporal activity, allowing for sustained modulation of macrophage behavior and redox homeostasis. Taken together, these results demonstrate that OH/PC/Ca^{2+} hydrogel exerts dual anti-inflammatory and antioxidative functions, primarily mediated by PC, while also promoting macrophage phenotype switching to M2. These immunological benefits, coupled with the material's physicochemical robustness, position it as a promising immunoactive platform for accelerating tissue repair and managing inflammatory microenvironments in clinical settings.

2.4. In Vivo Therapeutic Efficacy of OH/PC/Ca^{2+} Hydrogel in a Porcine Gastric ESD Model. To assess the clinical translatability of the OH/PC/Ca^{2+} hydrogel, we employed a porcine model of ESD, following a clinically relevant perioperative protocol (Figure 4a). Standard ESD procedure steps within the gastric antrum include lesion identification, submucosal injection, mucosal dissection, and wound observation (Figure S15). A conventional 0.4% HA solution containing 0.07% MB was used as the clinical control, while the test group received the OH/PC/Ca^{2+} hydrogel. Real-time endoscopic observation revealed that the HA/MB formulation induced an initial mucosal elevation that began to dissipate within 30 min and completely collapsed by 60 min. In contrast, the hydrogel maintained a stable submucosal lift throughout the entire operative window (Figure 4b), corroborating previous in vitro findings on injectability and mucosal elevation capacity. Standardized mucosal defects were subsequently created in both groups using a high-frequency electric knife. Notably, the HA/MB group required multiple reinjections during the procedure to sustain mucosal elevation, as the elevation rapidly diminished upon tissue incision. In sharp contrast, the OH/PC/Ca^{2+} hydrogel rapidly solidified in situ following a single injection, providing durable mechanical support without the need for additional administration. This sustained lift not only ensured continuous mucosal-muscularis propria separation but also simplified intraoperative handling and reduced the total operative time.

At 14 days postsurgery, animals were anesthetized and tissue samples from the gastric were harvested for histological and immunological evaluation (Figure S16). Following gastric dissection and flattening of the antral region, persistent mucosal defect wounds were observed in both the control group HA/MB (distal) and gel group OH/PC/Ca^{2+} (proximal), with adjacent mucosa actively contracting toward the lesion sites (Figure 4c). Hematoxylin and eosin (H&E) staining revealed granulation tissue filling the defect region in both groups (Figure 4e). To evaluate extracellular matrix remodeling, Sirius Red staining under white and polarized light was used to quantify collagen deposition. The collagen volume fraction in normal gastric mucosa was 25.9% ± 0.7%. While both HA/MB and hydrogel groups showed reduced collagen density—consistent with early stage tissue remodeling—the hydrogel group exhibited significantly higher collagen content (12.2% ± 0.9%) compared to the HA/MB group (8.3% ± 1.1%) (Figures 4e and S17). Polarized light microscopy revealed a predominant green birefringence in regenerated tissues, indicative of type III collagen fibers typical of

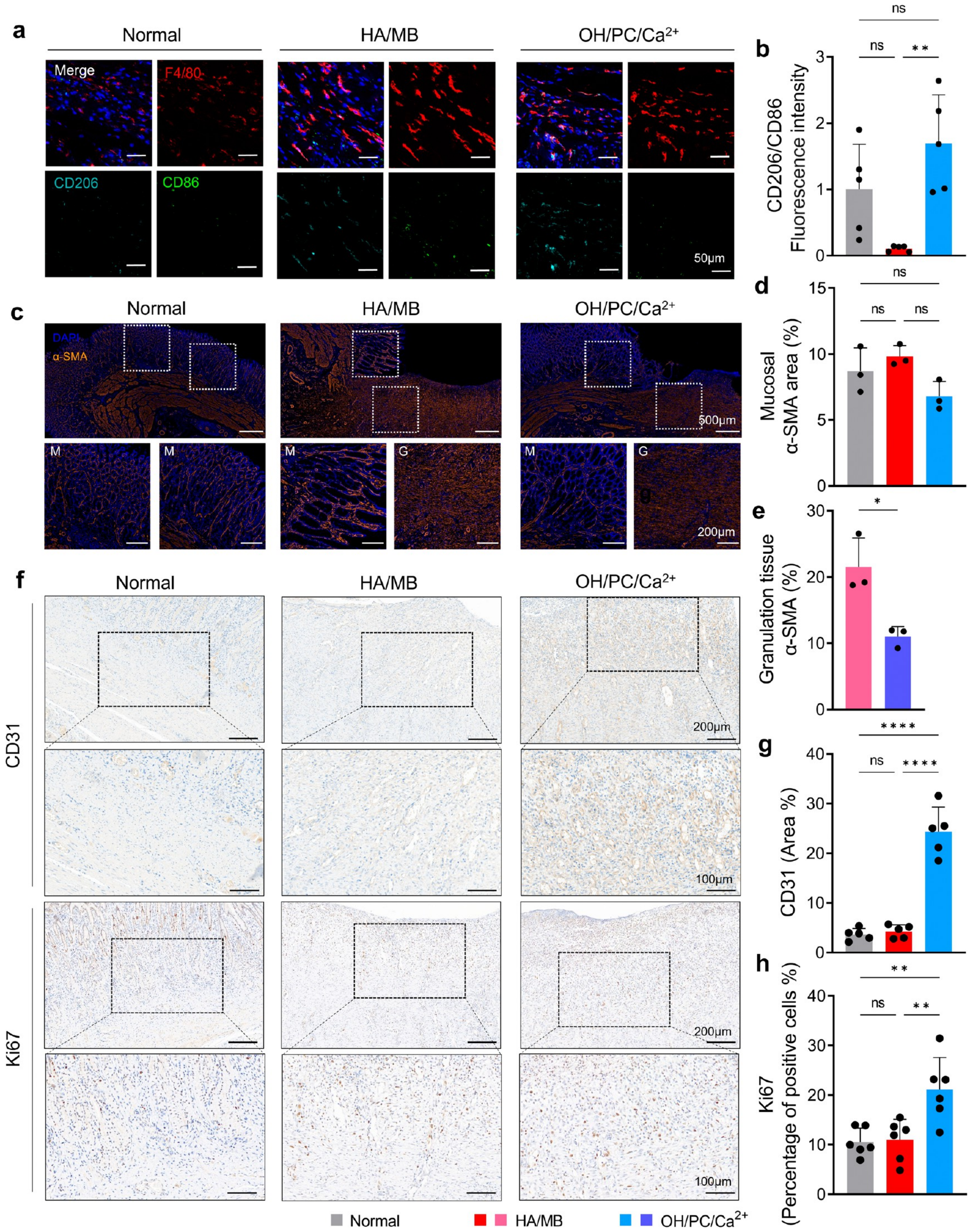

Figure 5. Immunomodulatory effects and histological assessment of gastric wound healing. (a) Immunofluorescent staining of macrophage phenotypes in gastric tissue on day 14 post-ESD. F4/80 (red, macrophage marker), CD206 (green, M2 marker), and CD86 (cyan, M1 marker). (b) Quantification of M2/M1 macrophage polarization ratio (CD206/CD86) ($n = 5$). (c) Representative α-SMA staining showing activated myofibroblasts in mucosa and granulation tissue. (d) Quantification of α-SMA-positive areas in the mucosal layer ($n = 3$). (e) Comparison of α-SMA expression in granulation tissue between HA and hydrogel groups ($n = 3$). (f) Immunohistochemical staining for

Figure 5. continued

CD31 (angiogenesis marker) and Ki67 (proliferation marker). (g,h) Quantitative analysis of CD31-positive area fraction and Ki67-positive cell percentages ($n = 5$). Data presented as mean ± SD. Statistical significance: ns = not significant, *$p < 0.05$, **$p < 0.01$, ***$p < 0.001$, ****$p < 0.0001$.

gastrointestinal mucosa. Notably, the spatial distribution and relative density of collagen observed under polarized light were consistent with those identified in the Sirius Red staining under white light (Figure 4f).

Next, we investigated the immunomodulatory effects of the hydrogel on macrophage polarization using immunofluorescence staining. Normal gastric tissue exhibited minimal macrophage infiltration, with negligible expression of polarization markers. In the HA group, F4/80$^+$ macrophages showed dominant CD86$^+$ (M1) expression, suggesting unresolved inflammation. In contrast, hydrogel-treated wounds showed significantly elevated CD206$^+$ (M2) expression, reflecting a shift toward a reparative immune microenvironment (Figure 5a,b).

To probe fibrotic remodeling, we examined α-smooth muscle actin (α-SMA) expression, a hallmark of activated myofibroblasts. Although no statistically significant differences were found in α-SMA expression within the mucosal layers of all three groups (Figure 5c,d), the granulation tissue in the HA group showed a significantly higher α-SMA-positive area (21.5% ± 4.4%) compared to the hydrogel group (11.0% ± 1.5%) (Figure 5e). This suggests that OH/PC/Ca^{2+} hydrogel may suppress persistent myofibroblast activation and thereby reduce the risk of fibrotic scarring.

Angiogenesis and cell proliferation were subsequently evaluated via CD31 and Ki67 immunohistochemistry (Figure 5f). The CD31$^+$ area in the hydrogel-treated wounds reached 24.4% ± 5.0%, substantially exceeding that of the HA (4.3% ± 1.3%) and normal groups (3.6% ± 1.2%), indicating potent pro-angiogenic activity (Figure 5g). Additionally, Ki67$^+$ cell density in the hydrogel group (21.1% ± 6.4%) was significantly greater than in the HA group (11.0% ± 4.1%), pointing to enhanced proliferative activity during tissue repair (Figure 5h). Collectively, these in vivo findings demonstrate that OH/PC/Ca^{2+} hydrogel not only maintains prolonged mucosal elevation and restrains excessive inflammation but also promotes organized tissue remodeling, suppresses fibrotic transition, and accelerates vascular and epithelial regeneration.

2.5. Validation of OH/PC/Ca^{2+} Hydrogel in a Porcine Esophageal ESD Model.

To evaluate the broader clinical applicability of the OH/PC/Ca^{2+} hydrogel beyond gastric interventions, we performed an in vivo ESD surgery in the midesophagus of pigs, following the same protocols, injection strategy, and analytical end points as employed in the gastric model. Remarkably, during the esophageal procedure, the hydrogel exhibited intrinsic hemostatic properties by effectively sealing submucosal vessels upon injection, as evidenced by real-time endoscopic observations (Supporting Video 1). At postoperative day 14, endoscopic examination revealed linear black scars at the resection sites in the hydrogel group, indicating complete wound closure and satisfactory epithelial regeneration (Figure S18). Histological analysis via H&E staining confirmed that, unlike gastric wounds which often remain partially uncovered, the esophageal wounds were re-epithelialized by this time point (Figures S19 and S20a), suggesting more advanced healing in the esophageal environment.

To assess extracellular matrix remodeling, Sirius Red staining under white light demonstrated a collagen volume fraction of 67.7 ± 7.5% in the lamina propria of normal esophageal mucosa, while the epithelial layer remained collagen-deficient, consistent with anatomical norms (Figure S20b,c). In the wound beds, the OH/PC/Ca^{2+} group exhibited significantly greater collagen deposition (41.7 ± 3.6%) than the HA/MB-treated controls (25.6 ± 1.8%), indicating enhanced matrix restoration. Under polarized light, collagen fibers in the hydrogel group displayed characteristic orange-red birefringence corresponding to well-organized type I collagen, which aligned closely with trends observed under white light (Figure S20d), confirming structural coherence in collagen reassembly.

Immunofluorescence analysis further explored macrophage polarization at the wound site. While the ratio of M2 (CD206$^+$) to M1 (CD86$^+$) macrophages did not achieve statistical significance, the hydrogel-treated group exhibited a consistent trend toward M2 predominance, mirroring findings in the gastric model (Figure S21a,b). This suggests a conserved immunoregulatory effect of the hydrogel in fostering a reparative microenvironment across gastrointestinal regions. In addition, α-SMA expression was examined to evaluate myofibroblast activation. Both the mucosal and granulation zones of HA/MB-treated wounds displayed significantly higher α-SMA levels compared to the hydrogel and normal groups (Figure S21c–e), indicating a heightened risk of fibrotic remodeling with conventional treatment. In contrast, the OH/PC/Ca^{2+} hydrogel group maintained relatively low α-SMA expression, supporting its antifibrotic potential.

In addition, immunohistochemical staining for CD31 and Ki67 preliminarily revealed trends consistent with gastric findings. Specifically, the hydrogel group demonstrated elevated neovascularization and cellular proliferation (Figure S21f–h), suggestive of accelerated and coordinated tissue regeneration. Collectively, the OH/PC/Ca^{2+} hydrogel exhibited consistent and favorable wound healing outcomes in both the stomach and esophagus. Its capabilities to achieve intraoperative hemostasis, support mucosal repair, regulate immune responses, organize collagen deposition, and promote angiogenesis position it as a highly promising injectable biomaterial for broad gastrointestinal ESD applications.

2.6. Translational Considerations and Future Directions.

This study introduces a clinically translatable injectable hydrogel composed of oxidized sodium alginate, carboxymethyl chitosan, and PC, reinforced through Ca^{2+}-mediated hybrid cross-linking. Compared with conventional injectates like normal saline or hyaluronic acid, the OH/PC/Ca^{2+} hydrogel offers durable mucosal elevation, rapid in situ gelation, and integrated postoperative immunomodulatory functions. Its shear-thinning and self-healing behavior allow delivery through fine endoscopic needles and stable retention under gastrointestinal motility.

Beyond physical performance, the hydrogel provides antioxidant and anti-inflammatory benefits via sustained phycocyanin release. Unlike synthetic dyes such as methylene blue, PC serves as both a visual contrast agent and a bioactive component, simplifying formulation while enhancing therapeutic effect. In vivo porcine models demonstrated prolonged mucosal lifting, shortened procedural time, and accelerated epithelial and collagen regeneration, suggesting robust efficacy across distinct gastrointestinal locations.

PC, a natural pigment–protein with established antioxidant and anti-inflammatory properties, has been investigated in clinical studies for the management of periodontitis,[62] oral submucosal fibrosis,[63] wound healing after periodontal flap surgery,[64] asthma,[65] Alzheimer,[66] and hypertension.[67] However, its use as a therapeutic agent in injectable biomaterials necessitates more rigorous evaluation. When delivered submucosally, the hydrogel matrix offers a sustained-release environment that may mitigate acute immune responses, and exposure to digestive enzymes may further limit systemic absorption. Nevertheless, thorough immunogenicity profiling, biodistribution studies, and dose-dependent safety assessments remain essential to support regulatory approval and clinical application.

To advance this platform toward clinical use, several future efforts are necessary. Validation in colorectal ESD models will be critical to confirm performance across the full range of gastrointestinal anatomies. Longer-term animal studies should assess wound remodeling, fibrotic response, and hydrogel degradation dynamics beyond the 14 day window used in the current work. Additionally, establishing a GMP-compliant manufacturing process, including control of key quality attributes such as viscosity, gelation time, and bioactive content, is a crucial step toward clinical-grade production. Early engagement with regulatory agencies and well-designed toxicological studies will be equally important in defining a feasible translational pathway. Collectively, these future directions will lay the foundation for the safe, scalable, and clinically effective application of OH/PC/Ca^{2+} hydrogel in therapeutic endoscopy.

3. CONCLUSIONS

In this study, we developed a multifunctional injectable hydrogel based on oxidized sodium alginate, carboxymethyl chitosan, and phycocyanin, reinforced with Ca^{2+}-mediated dual cross-linking, for application in ESD. Comprehensive in vitro assessments demonstrated the hydrogel's robust mechanical integrity, environmental adaptability, tissue adhesiveness, and sustained PC release. Cellular assays confirmed excellent cytocompatibility and hemocompatibility, while dynamic macrophage polarization and ROS suppression assays highlighted the hydrogel's immunomodulatory and redox-scavenging properties. In clinically relevant porcine models of gastric and esophageal ESD, the hydrogel provided durable mucosal elevation without reinjection, reduced total operative time, and organized collagen regeneration, angiogenesis, and epithelial proliferation, while attenuating myofibroblast activation and fibrotic remodeling. Its consistent performance across different anatomical regions underscores its robustness and translational potential. Altogether, the OH/PC/Ca^{2+} hydrogel offers an integrated platform that combines mechanical support, visual enhancement, and localized immunomodulation in a single injectable system. This work lays the foundation for next-generation submucosal injection materials aimed at improving surgical precision, reducing complication rates, and accelerating mucosal repair in minimally invasive gastrointestinal procedures.

4. METHODS

4.1. Synthesis of OSA. OSA was synthesized via periodate-mediated selective cleavage of vicinal diols on the alginate backbone. Briefly, 10 g of sodium alginate was dissolved in 250 mL of ultrapure water under continuous magnetic stirring at ambient temperature until fully solubilized. To initiate oxidation, 10.8 g of sodium periodate ($NaIO_4$) was added (alginate:oxidant mass ratio = 1:1.08), and the reaction mixture was maintained at 25 °C in the dark for 8 h to prevent photodegradation and side reactions. Following oxidation, 10 mL of ethylene glycol was introduced to quench residual periodate and terminate the reaction. The resulting solution was dialyzed (MWCO 3500 Da) against ultrapure water for 72 h, with water changes every 4–6 h to remove unreacted reagents and low-molecular-weight byproducts. The dialyzed product was subsequently lyophilized to yield a dry, porous OSA powder suitable for downstream hydrogel formulation.

4.2. Characterization. The chemical structure of the synthesized materials was analyzed by Fourier-transform infrared spectroscopy (FTIR) in transmission mode, using a spectral range of 4000–400 cm^{-1}. Each spectrum was acquired with a resolution of 4 cm^{-1} and averaged over 32 scans to ensure high signal-to-noise ratio and spectral fidelity. To evaluate the microstructure of the lyophilized hydrogels, scanning electron microscopy (SEM) was performed. Samples were sputter-coated with a thin layer of gold prior to imaging to enhance surface conductivity and resolution. Morphological assessment focused on porosity, network architecture, and surface topography.

4.3. Calculation of Oxidation Degree. The degree of oxidation of OSA was quantified using a hydroxylamine hydrochloride-based titration assay. First, 4.375 g of hydroxylamine hydrochloride was dissolved in 37.5 mL of deionized water. After complete dissolution, 1.5 mL of 0.05% (w/v) methyl orange indicator was added, and the solution was diluted to a final volume of 250 mL. The pH was adjusted to 4.0 using standardized buffer solutions. Next, 0.1 g of OSA was dissolved in 25 mL of the prepared reagent mixture and incubated at room temperature in the dark for 2 h to allow complete reaction between aldehyde groups and hydroxylamine. The resulting oxime reaction mixture was titrated with 0.1 M sodium hydroxide (NaOH) until the end point was reached, indicated by a color change from red to yellow. The oxidation degree (OD) was calculated using the following formula

$$\begin{aligned}\text{Oxidation degree(OD)} &= \frac{m_{\text{CHO}}}{m(\text{OSAunit})}\\ &= \frac{C_{\text{NaOH}} \times V_{\text{NaOH}}/2}{m(\text{OSA})/M(\text{OSAunit})} \times 100\%\end{aligned}$$

where C_{NaOH} and V_{NaOH} represent the molarity (mol/L) and volume (L) of NaOH consumed, respectively. m_{CHO} denotes the calculated mass of aldehyde groups per unit mass of OSA. $m(\text{OSA})$is the mass of OSA (g). $M(\text{OSAunit})$ is the molar mass of a repeating unit in OSA (198.10 g/mol).

4.4. Preparation of OSA/CMCS Hydrogels. Hydrogel Combinatorial Library: OSA was dissolved in deionized water at concentrations of 3%, 4%, and 5% (w/v), designated as 3O, 4O, and 5O, respectively. Separately, CMCS was also dissolved at 3%, 4%, and 5% (w/v), labeled as 3C, 4C, and 5C. All polymer solutions were adjusted to a neutral pH of 7.0. The hydrogels were fabricated by mixing OSA and CMCS solutions at three different volume ratios: 1:2, 1:1, and 2:1 (V(OSA)/V(CMCS)), following an orthogonal experimental design to systematically explore formulation space. Each formulation was denoted as xOyC-R (e.g., 3O3C-1/2, 4O5C-2/1), yielding a total of 27 unique hydrogel combinations.

Optimized Hydrogel (OH) and PC-Loaded Variant (OH/PC): based on rheological and injectability screening, the formulation combining 4% OSA and 3% CMCS at a volume ratio of 1:2 (4O3C-1/2) was identified as optimal and referred to as the "Optimal Hydrogel" (OH). PC was incorporated at a final concentration of 1%

(w/v) during hydrogel blending to obtain a bioactive variant denoted as OH/PC.

Calcium Ion-Reinforced Hydrogel (OH/PC/Ca^{2+}): To enhance mechanical strength and tissue adhesion, a 1% (w/v) aqueous calcium chloride ($CaCl_2$) solution was prepared and premixed with the 3% CMCS solution. The OH/PC/Ca^{2+} hydrogel was formulated by blending 4% OSA, 3% CMCS, and 1% $CaCl_2$ solutions at a volumetric ratio of 2:4:1, with PC uniformly loaded at 1% (w/v).

4.5. Gelation Time Assessment. To simulate physiological conditions, all precursor solutions were pre-equilibrated at 37 °C in a thermostatically controlled incubator. Gelation was initiated by mixing OSA and CMCS (with or without Ca^{2+} or PC, as applicable) directly in transparent centrifuge tubes placed on a magnetic stirrer to ensure uniform mixing. The tubes were manually inverted at 10 s intervals to monitor the sol−gel transition. The gelation time was defined as the point at which the hydrogel no longer flowed or detached from the bottom of the tube upon inversion. For statistical validation, each formulation was tested in triplicate, and the mean gelation time with standard deviation was calculated.

4.6. Measurement of Injection Resistance. Injection resistance was evaluated using a custom-designed extrusion apparatus simulating clinical endoscopic injection conditions. The system consisted of a 1.5 m infusion tube (inner diameter: 2 mm) connected to a standard 20-gauge needle (aperture: 0.9 mm) to mimic the anatomical delivery route. A constant extrusion force of 9.8 N was applied via a vertically loaded 1 kg weight mounted on the plunger of a 10 mL syringe. Each hydrogel precursor formulation (6 mL) was loaded into the syringe and extruded under sustained pressure. The volume of material extruded at 1, 2, and 3 min was recorded. Injection resistance was inversely correlated with the extruded volume; lower resistance allowed for greater material delivery. All measurements were performed in triplicate, and results were reported as mean ± standard deviation.

4.7. Evaluation of Self-Healing Capability. The macroscopic self-healing behavior of the OH/PC/Ca^{2+} hydrogel was assessed using both visual observation and rheological testing. In the first demonstration, a heart-shaped construct was fabricated by manually juxtaposing two semicircular hydrogel segments: one composed of colorless OH/Ca^{2+} hydrogel, and the other infused with 1% (w/v) PC, imparting a blue hue (OH/PC/Ca^{2+}). Upon alignment, the two segments autonomously bonded at the interface within minutes at room temperature, forming an integrated structure without the need for external triggers, indicating spontaneous interfacial self-repair. For a more rigorous assessment, both hydrogel types were separately fragmented into fine pieces using a sterile scalpel. Equal amounts of each were mixed thoroughly and transferred into circular molds, allowing for reassembly and network reformation under static conditions at 25 °C for 2 h.

To quantitatively evaluate dynamic self-healing properties, oscillatory rheology was conducted on the reconstituted hydrogels using a strain step test protocol. The strain amplitude was cyclically alternated between low (γ = 1%, representing the linear viscoelastic region) and high deformation (γ = 200%, inducing structural disruption) at a constant angular frequency of 1 Hz. This cycle was repeated five times to assess recovery behavior across repeated mechanical challenges.

4.8. In Vitro Degradation Assessment. Hydrogels were formed in cylindrical molds and incubated in 10 mL of PBS or dilute hydrochloric acid (pH = 2.4). Samples were retrieved at 0, 12, 24, and 36 h postincubation. For each time point, three parallel specimens were analyzed to ensure reproducibility. Following removal, residual hydrogels were gently rinsed, lyophilized, and weighed. The degradation rate was calculated based on the change in mass using the following formula

$$\text{Degtadation rate}(\%) = \frac{W_t - W_0}{W_0} \times 100\%$$

whereW_t and W_0 represent weight of the degraded sample and the initial sample, respectively. All data were reported as mean ± standard deviation from triplicate measurements.

4.9. In Vitro Release Kinetics of PC. To quantify the release behavior of PC from the hydrogel matrix, a standard calibration curve was first constructed. A series of PC standard solutions (0.6, 0.8, 1.0, 1.2, and 1.4 mg/mL) were prepared in 0.9% saline, and their UV−vis spectra were recorded to identify the characteristic absorbance peak at 622 nm. The linear relationship between absorbance and concentration enabled conversion of optical data to PC concentrations. Hydrogels containing 1% (w/v) PC were prepared in cylindrical molds and immersed in 10 mL of 0.9% NaCl solution at 37 °C. At predetermined time intervals, 2 mL aliquots of the release medium were withdrawn and immediately replenished with an equal volume of fresh saline to maintain sink conditions and constant volume. Absorbance of collected supernatants at 622 nm was measured, and PC concentration was calculated using the standard curve. The cumulative release (%) of phycocyanin at each time point was determined using the following equation

$$\text{Cr} = \frac{V_0 \times \rho_t + V \times \sum_{i=1}^{t-1} \rho_i}{m} \times 100\%$$

where V_0 is the total volume of release medium (mL), V is the volume withdrawn per sampling (2 mL), $\rho_t$is the PC concentration at time t (mg/mL), ρ_i is the PC concentration at earlier time points (mg/mL), and m is the total amount of PC initially loaded into the hydrogel (mg).

4.10. DPPH (2,2-Diphenyl-1-picrylhydrazyl) Radical Scavenging Assay. The antioxidant capacity of PC and PC-loaded hydrogels was evaluated via the DPPH radical scavenging assay. PC solutions were freshly prepared in PBS at concentrations of 1.00% (w/v). Correspondingly, the extract was obtained by immersing the OH/PC/Ca^{2+} hydrogels (0.1 g/mL)) in PBS for 48 h. The assay was conducted in a 96-well microplate under the following groups:

Sample Group (A_{Sample}): 100 μL of test solution (either PC or hydrogel) mixed with 100 μL of 0.2 mM DPPH solution in absolute ethanol.

Sample Blank (A_{Blank1}): 100 μL of test solution mixed with 100 μL of absolute ethanol (to correct for background absorbance).

Solvent Control (A_{Blank2}): 100 μL of absolute ethanol mixed with 100 μL of DPPH solution (representing maximum radical signal).

The mixtures were incubated in the dark at 25 °C for 30 min to prevent photodegradation. Absorbance was then measured at 517 nm using a microplate reader. The percentage of DPPH radical scavenging activity was calculated according to the following equation

$$\text{Scavenging activity } (\%) = \left(1 - \frac{A_{\text{Sample}} - A_{\text{Blank1}}}{A_{\text{Blank2}}}\right) \times 100\%$$

4.11. Adhesive Shear Strength Evaluation. The adhesive properties of the hydrogel formulations were quantitatively evaluated using a universal testing machine operating at a crosshead speed of 5 mm/min, configured in shear mode. Fresh porcine skin specimens (5.0 cm × 1.5 cm) were pretreated by immersion in simulated gastric fluid (pH 1.5) at 37 °C for 1.5 h to emulate physiologically relevant conditions. Following equilibration, 50 μL of hydrogel was applied to a 1.0 cm × 1.5 cm contact interface between two hydrated skin substrates. The specimens were gently pressed to ensure uniform contact and allowed to stabilize for 10 min prior to mechanical testing. The maximum shear force (F) required to separate the bonded tissues was recorded. Adhesive shear strength (Pa, in N/m^2) was calculated using the following formula

$$\text{Pa} = \frac{N}{m^2} = \frac{F}{W \times L}$$

where F represents maximum detachment force (N), W is the width of the adhesive interface (m), and L is length of the adhesive interface.

4.12. Coagulation Assay. To evaluate the hemostatic potential of the hydrogel, a rat whole blood coagulation model was employed.

Fresh whole blood was collected into tubes preloaded with 3.8% (w/v) sodium citrate solution at a citrate-to-blood volume ratio of 1:9 to prevent premature clotting. For each assay, 300 μL of recalcified blood was prepared by combining 250 μL of citrated blood with 50 μL of 25 mM calcium chloride ($CaCl_2$) to restore coagulation capacity. This recalcified blood was immediately transferred into sample vials containing preformed hydrogels. Tubes were gently inverted at regular intervals to assess fluidity. The end point was defined as the cessation of visible flow, at which point coagulation time was recorded. Blood without any hydrogel served as the negative control, establishing baseline coagulation kinetics.

4.13. Ex Vivo Submucosal Elevation Assessment in Porcine Gastric Tissue. To evaluate the injectability and in situ retention of the hydrogel under ESD-relevant conditions, an ex vivo model was established using freshly excised porcine stomach tissue. A total of 2 mL of either 0.4% (w/v) HA solution or the optimized OH/PC/Ca^{2+} hydrogel was injected into the submucosal layer via a clinical-grade endoscopic needle, following a standardized injection procedure. The resulting mucosal elevation was immediately assessed using a high-precision digital caliper (resolution: 0.01 mm) to determine the baseline elevation height (H_0). To quantify the temporal stability of the mucosal lift, the height of the submucosal bulge (H_t) was recorded at 30, 60, 90, and 120 min postinjection. All measurements were normalized to the initial height, and the retention of submucosal elevation was expressed as percentage retention

$$\text{Heigh tretention rate (\%)} = \frac{H_t - H_0}{H_0} \times 100\%$$

4.14. Diffusion Behavior Analysis. To investigate the molecular diffusion behavior of dye- and protein-loaded hydrogel systems, four formulations were prepared and assessed: (1) sodium hyaluronate solution (0.4%, w/v) containing methylene blue (0.07%, w/v), denoted as HA/MB; (2) oxidized hydrogel incorporating methylene blue and calcium ions, OH/MB/Ca^{2+}; (3) phycocyanin-loaded oxidized hydrogel with calcium ions, OH/PC/Ca^{2+}. Each sample (200 μL) was carefully injected into the bottom of a 1.5 mL Eppendorf tube prefilled with PBS (pH 7.4), creating a well-defined interface for upward diffusion. The tubes were maintained at room temperature under static conditions. At designated time points, images were captured from a fixed vertical angle using a calibrated digital imaging system. The diffusion distance of MB and PC into the PBS medium was measured using ImageJ software, based on contrast thresholds and pixel-based linear calibration.

4.15. Cytotoxicity. In vitro cytocompatibility of the PC and hydrogel formulations was assessed using the Cell Counting Kit-8 (CCK-8) assay in accordance with ISO 10993-5 guidelines for biological evaluation of medical devices. Murine NIH/3T3 fibroblasts were seeded into 96-well tissue culture plates at a density of 3000 cells/well and cultured under standard conditions (37 °C, 5% CO_2) for 24 h to allow for cell attachment. Test solutions included serial concentrations of free PC (2, 1, 0.5, 0.25, and 0.125 mg/mL) and extracts from OH/Ca^{2+} and OH/PC/Ca^{2+} hydrogels, prepared by immersing 0.1 g/mL of hydrogel in complete culture medium for 48 h at 37 °C, followed by 0.22 μm sterile filtration. Cells were then exposed to these extracts for 24 h. Subsequently, 10% (v/v) CCK-8 reagent was added to each well, and plates were incubated for 2 h at 37 °C. The absorbance was measured at 450 nm using a microplate spectrophotometer. Cell viability was expressed as a percentage relative to untreated controls. All conditions were tested in triplicate wells and repeated in three independent biological replicates.

4.16. Hemolysis Assay. To assess the hemocompatibility of the hydrogel formulations, a standard hemolysis assay was performed using heparinized rat blood. Whole blood was centrifuged to isolate erythrocytes, followed by a 1:9 dilution (v/v) of red blood cells in PBS. For each test, 300 μL of the diluted erythrocyte suspension was added to 300 μL of hydrogel. Deionized water and PBS served as the positive and negative controls, respectively. After incubation at 37 °C for 1 h, all samples were centrifuged at 2500 rpm for 5 min. The absorbance of the supernatant was measured at 540 nm using a microplate reader to quantify the extent of hemoglobin release. The hemolysis ratio (%) was calculated using the following equation

$$\text{Hemolysis (\%)} = (\text{OD}_{\text{Sample}} - \text{OD}_{\text{Negative}}) / (\text{OD}_{\text{Positive}} - \text{OD}_{\text{Negative}}) \times 100\%$$

4.17. In Vitro Macrophage Polarization Assay. To evaluate the immunomodulatory capacity of phycocyanin and hydrogel formulations, an in vitro macrophage polarization model was established using RAW 264.7 murine macrophages. Cells were seeded in 6-well plates at a density of 5×10^5 cells/well and pretreated with lipopolysaccharide (LPS, 100 ng/mL) to induce M1 polarization. Following stimulation, cells were cocultured for 24 h with one of the following treatments: PC solution (200 μg/mL), OH/Ca^{2+} hydrogels, or OH/PC/Ca^{2+} hydrogels. After incubation, cells were harvested, washed with PBS, and stained with a panel of fluorescently conjugated antibodies: F4/80-FITC (macrophage marker), CD86-PE-Cy7 (M1 marker), and CD206-APC (M2 marker). Surface marker expression was assessed by multicolor flow cytometry using a BD FACSCanto II cytometer. For ROS detection, cells were loaded with 2′,7′-dichlorodihydrofluorescein diacetate (DCFH-DA) for 30 min at 37 °C. Following probe incubation, cells analyzed by flow cytometry using the FITC channel. In parallel, culture supernatants were collected to quantify the secretion of TNF-α and IL-6 using commercially available ELISA kits, following the manufacturer's protocols. Additionally, NO levels were determined using a Griess reagent-based colorimetric assay to evaluate reactive nitrogen species production as a surrogate marker of inflammatory activation.

4.18. ESD in Porcine Models. To evaluate the translational efficacy of the hydrogel formulation, a porcine model of ESD was established using 15 month-old domestic pigs (*Sus scrofa* domesticus, average body weight ∼70 kg). Animals were fasted for 48 h prior to surgery to ensure optimal gastrointestinal conditions. Under general anesthesia, pigs were positioned supine with oral access secured via jaw fixation to facilitate endoscope maneuverability. Two submucosal injection cohorts were designated: control group (0.4% sodium hyaluronate solution) and experimental group (OH/PC/Ca^{2+} hydrogel). Injection sites in the gastric or esophageal mucosa were spaced at $\geq$ 3 cm intervals to avoid overlapping diffusion or intergroup interference. Submucosal elevation dynamics were continuously monitored under real-time endoscopy, with image documentation acquired every 5 min up to 60 min postinjection. ESD was performed using a high-frequency electrosurgical knife, generating consistent mucosal lesions measuring 2.0 × 2.0 cm across all specimens. Throughout the procedure, vital parameters including heart rate and respiratory rate were closely monitored. Following surgery, animals were fasted for an additional 24 h, then transitioned to a liquid diet supplemented with enteral nutrition, broad-spectrum antibiotics, and proton pump inhibitors (PPIs). This postoperative regimen was maintained for 7 days, continuing until euthanasia on postoperative day 14. Upon euthanasia, tissue specimens encompassing the wound sites and adjacent normal mucosa were carefully excised. Samples were fixed in 10% neutral-buffered formalin, embedded in paraffin, and sectioned at 4 μm thickness for subsequent histopathological and immunohistochemical evaluations.

4.19. Statistical Analysis. All quantitative data are expressed as mean ± standard deviation (SD). Statistical analyses were performed using GraphPad Prism (version 9.5.1). One-way analysis of variance (ANOVA) was employed for comparisons among multiple groups. Statistical significance: ns = not significant, $^{*}p < 0.05$, $^{**}p < 0.01$, $^{***}p < 0.001$, $^{****}p < 0.0001$.

4.20. Statement. All animal procedures were conducted in accordance with guidelines approved by the Ethics Committee of Soochow University (Soochow, China), approval number 202309A0232.

ASSOCIATED CONTENT

Supporting Information

The Supporting Information is available free of charge at https://pubs.acs.org/doi/10.1021/acsnano.5c14055.

Characterization of oxidized sodium alginate; photograph of the endoscopic submucosal injection needle used in clinical procedures; inversion-tube method for measuring hydrogel gelation time; custom-designed vertical injection apparatus; FTIR spectra of hydrogels with different compositions; SEM micrographs of freeze-dried hydrogels; self-healing behavior of hydrogels; UV–Vis absorption spectra of phycocyanin at different concentrations; adhesion of OH/PC/Ca^{2+} hydrogel to porcine tissues; lap shear adhesion profiles of OH/PC and OH/PC/Ca^{2+} hydrogels on porcine skin; ex vivo porcine stomach model used to evaluate mucosal lifting height; hemolysis assay results of various formulations; immunomodulatory and antioxidant effects of OH/Ca^{2+} hydrogel on LPS-stimulated macrophages; MDA concentrations as a marker of lipid peroxidation; standard ESD procedure steps; excised gastric specimens harvested 14 days postoperation; quantitative analysis of collagen volume fraction in normal tissue, HA-treated, and hydrogel-treated wounds based on Sirius Red staining; endoscopic follow-up of esophageal ESD wounds at postoperative day 14; histological comparison of normal gastrointestinal mucosa; histological and collagen analysis of esophageal ESD wounds; immunofluorescence and immunohistochemical analysis of esophageal wound healing; orthogonal experimental table (PDF)

Supporting Video 1 (MP4)

AUTHOR INFORMATION

Corresponding Authors

Yongyou Wu − *Department of General Surgery, The Second Affiliated Hospital of Soochow University, Suzhou 215004, China*; Email: wuyoyo@aliyun.com

Jianfeng Zeng − *Department of Radiology, The First Affiliated Hospital of Soochow University, State Key Laboratory of Radiation Medicine and Protection, School for Radiological and Interdisciplinary Sciences (RAD-X), Collaborative Innovation Center of Radiological Medicine of Jiangsu Higher Education Institutions, Soochow University, Suzhou 215123, China; Department of General Surgery, The Second Affiliated Hospital of Soochow University, Suzhou 215004, China*; orcid.org/0000-0001-7654-8724; Email: jfzeng@suda.edu.cn

Mingyuan Gao − *Department of Radiology, The First Affiliated Hospital of Soochow University, State Key Laboratory of Radiation Medicine and Protection, School for Radiological and Interdisciplinary Sciences (RAD-X), Collaborative Innovation Center of Radiological Medicine of Jiangsu Higher Education Institutions, Soochow University, Suzhou 215123, China; Institute of Biomedical Engineering, School of Life Sciences, Suzhou Medical College of Soochow University, Suzhou 215123, China*; orcid.org/0000-0002-7360-3684; Email: gaomy@suda.edu.cn

Authors

Mengdan Xu − *Department of Radiology, The First Affiliated Hospital of Soochow University, State Key Laboratory of Radiation Medicine and Protection, School for Radiological and Interdisciplinary Sciences (RAD-X), Collaborative Innovation Center of Radiological Medicine of Jiangsu Higher Education Institutions, Soochow University, Suzhou 215123, China*; orcid.org/0009-0002-4544-4046

Wei Peng − *Department of General Surgery, The Second Affiliated Hospital of Soochow University, Suzhou 215004, China*

Guangqiu Yu − *Department of General Surgery, The Second Affiliated Hospital of Soochow University, Suzhou 215004, China*

Zixuan Xiao − *Department of Radiology, The First Affiliated Hospital of Soochow University, State Key Laboratory of Radiation Medicine and Protection, School for Radiological and Interdisciplinary Sciences (RAD-X), Collaborative Innovation Center of Radiological Medicine of Jiangsu Higher Education Institutions, Soochow University, Suzhou 215123, China*

Zhongsheng Zhao − *Department of Radiology, The First Affiliated Hospital of Soochow University, State Key Laboratory of Radiation Medicine and Protection, School for Radiological and Interdisciplinary Sciences (RAD-X), Collaborative Innovation Center of Radiological Medicine of Jiangsu Higher Education Institutions, Soochow University, Suzhou 215123, China*

Zelong Xu − *Department of General Surgery, The Second Affiliated Hospital of Soochow University, Suzhou 215004, China*

Qiankun Shao − *Department of General Surgery, The Second Affiliated Hospital of Soochow University, Suzhou 215004, China*

Xiuqi Hu − *Department of Radiology, The First Affiliated Hospital of Soochow University, State Key Laboratory of Radiation Medicine and Protection, School for Radiological and Interdisciplinary Sciences (RAD-X), Collaborative Innovation Center of Radiological Medicine of Jiangsu Higher Education Institutions, Soochow University, Suzhou 215123, China*

Zeyuan Cao − *Department of General Surgery, The Second Affiliated Hospital of Soochow University, Suzhou 215004, China*

Mengyao Wu − *Department of Radiology, The First Affiliated Hospital of Soochow University, State Key Laboratory of Radiation Medicine and Protection, School for Radiological and Interdisciplinary Sciences (RAD-X), Collaborative Innovation Center of Radiological Medicine of Jiangsu Higher Education Institutions, Soochow University, Suzhou 215123, China*

Xiao Xiao − *Department of Radiology, The First Affiliated Hospital of Soochow University, State Key Laboratory of Radiation Medicine and Protection, School for Radiological and Interdisciplinary Sciences (RAD-X), Collaborative Innovation Center of Radiological Medicine of Jiangsu Higher Education Institutions, Soochow University, Suzhou 215123, China*

Yadan Shi − *Department of Radiology, The First Affiliated Hospital of Soochow University, State Key Laboratory of Radiation Medicine and Protection, School for Radiological and Interdisciplinary Sciences (RAD-X), Collaborative Innovation Center of Radiological Medicine of Jiangsu Higher Education Institutions, Soochow University, Suzhou 215123, China*

Complete contact information is available at: https://pubs.acs.org/10.1021/acsnano.5c14055

Author Contributions

‖M.X, W.P., and G.Y. contributed equally. The manuscript was written through contributions of all authors. All authors have given approval to the final version of the manuscript.

Notes

The authors declare no competing financial interest.

ACKNOWLEDGMENTS

The authors are thankful for the financial support from the National Natural Science Foundation of China (82222033, 82572396, 82130059, 82172003), Suzhou Fundamental Research Project (SJC2023001), and Priority Academic Program Development of Jiangsu Higher Education Institutions (PAPD). Scheme 1a,b, Figure 2k, Figure 3a, and Figure 4a,c were created with BioRender.com.

REFERENCES

(1) Chiu, P. W. Y.; Uedo, N.; Singh, R.; Gotoda, T.; Ng, E. K. W.; Yao, K.; Ang, T. L.; Ho, S. H.; Kikuchi, D.; Yao, F.; Pittayanon, R.; Goda, K.; Lau, J. Y. W.; Tajiri, H.; Inoue, H. An Asian consensus on standards of diagnostic upper endoscopy for neoplasia. *Gut* **2019**, *68*, 186.

(2) Hoffman, A.; Atreya, R.; Rath, T.; Neurath, M. Current Endoscopic Resection Techniques for Gastrointestinal Lesions: Endoscopic Mucosal Resection, Submucosal Dissection, and Full-Thickness Resection. *Visc. Med.* **2021**, *37*, 358−371.

(3) Libânio, D.; Pimentel-Nunes, P.; Bastiaansen, B.; Bisschops, R.; Bourke, M. J.; Deprez, P. H.; Esposito, G.; Lemmers, A.; Leclercq, P.; Maselli, R.; Messmann, H.; Pech, O.; Pioche, M.; Vieth, M.; Weusten, B. L. a.M.; Fuccio, L.; Bhandari, P.; Dinis-Ribeiro, M. Endoscopic submucosal dissection techniques and technology: European Society of Gastrointestinal Endoscopy (ESGE) Technical Review. *Endoscopy* **2023**, *55*, 361−389.

(4) Kita, H.; Yamamoto, H.; Miyata, T.; Sunada, K.; Iwamoto, M.; Yano, T.; Yoshizawa, M.; Hanatsuka, K.; Arashiro, M.; Omata, T.; Sugano, K. Endoscopic submucosal dissection using sodium hyaluronate, a new technique for en bloc resection of a large superficial tumor in the colon. *Inflammopharmacology* **2007**, *15*, 129−131.

(5) Yandrapu, H.; Desai, M.; Siddique, S.; Vennalganti, P.; Vennalaganti, S.; Parasa, S.; Rai, T.; Kanakadandi, V.; Bansal, A.; Titi, M.; Repici, A.; Bechtold, M. L.; Sharma, P.; Choudhary, A. Normal saline solution versus other viscous solutions for submucosal injection during endoscopic mucosal resection: a systematic review and meta-analysis. *Gastrointest. Endosc* **2017**, *85*, 693−699.

(6) Jung, Y. S.; Park, D. I. Submucosal injection solutions for endoscopic mucosal resection and endoscopic submucosal dissection of gastrointestinal neoplasms. *Gastrointest. Interv.* **2013**, *2*, 73−77.

(7) Yamamoto, H.; Kawata, H.; Sunada, K.; Satoh, K.; Kaneko, Y.; Ido, K.; Sugano, K. Success rate of curative endoscopic mucosal resection with circumferential mucosal incision assisted by submucosal injection of sodium hyaluronate. *Gastrointest. Endosc* **2002**, *56*, 507−512.

(8) Fujishiro, M.; Yahagi, N.; Kashimura, K.; Mizushima, Y.; Oka, M.; Enomoto, S.; Kakushima, N.; Kobayashi, K.; Hashimoto, T.; Iguchi, M.; Shimizu, Y.; Ichinose, M.; Omata, M. Comparison of various submucosal injection solutions for maintaining mucosal elevation during endoscopic mucosal resection. *Endoscopy* **2004**, *36*, 579−583.

(9) Tan, B.; Wang, J. H.; Wu, Q. D.; Kirwan, W. O.; Redmond, H. P. Sodium hyaluronate enhances colorectal tumour cell metastatic potential in vitro and in vivo. *Br. J. Surg.* **2001**, *88*, 246−250.

(10) Rex, D. K.; Broadley, H. M.; Garcia, J. R.; Lahr, R. E.; Macphail, M. E.; Mcwhinney, C. D.; Searight, M. P.; Sullivan, A. W.; Mahajan, N.; Eckert, G. J.; Vemulapalli, K. C. SIC-8000 versus hetastarch as a submucosal injection fluid for EMR: a randomized controlled trial. *Gastrointest. Endosc* **2019**, *90*, 807−812.

(11) Giannino, V.; Salandin, L.; Macelloni, C.; Longo, L. M. Evaluation of Eleview® Bioadhesive Properties and Cushion-Forming Ability. *Polymers* **2020**, *12*, 346.

(12) Sun, B. L. Submucosal lifting agent ORISE gel causes extensive foreign body granuloma post endoscopic resection. *Int. J. Colorectal Dis* **2021**, *36*, 419−422.

(13) Dong, Z. M.; Fang, J.; Byrne, K. R.; Bronner, M. P.; Hale, G. L. Histologic mimics and diagnostic pitfalls of gastrointestinal endoscopic lifting media, ORISE gel and Eleview®. *Hum. Pathol.* **2022**, *119*, 28−40.

(14) Alipouriani, A.; Elsoukkary, S. S.; Erozkan, K.; Sommovilla, J.; Bhatt, A.; Valente, M. A.; Steele, S. R.; Gorgun, E. Adverse tissue reactions to ORISE gel during endoscopic mucosal resection and dissection. *J. Gastrointest. Surg.* **2024**, *28*, 1963−1969.

(15) Xu, M.; Xu, K.; Peng, W.; Ge, J.; Wang, N.; Yu, G.; Wu, Y.; Zeng, J. Hydrogels in endoscopic submucosal dissection for gastrointestinal cancers. *Acta Biomater.* **2025**, *200*, 47−66.

(16) Xu, R. F.; Yang, X. Y.; Yi, T.; Tan, T.; Li, Z. Q.; Feng, X. Y.; Rao, J.; Zhou, P. H.; Hu, H.; Zhan, Y. H. Injectable temperature-sensitive hydrogel facilitating endoscopic submucosal dissection. *Front. Bioeng. Biotechnol.* **2024**, *12*, 1395731.

(17) Ma, J. P.; Wang, P. H.; Tang, C. F.; Liao, H. Y.; Zhang, W. J.; Yang, R.; Shi, T. Q.; Tan, X. Y.; Chi, B. Injectable shear-thinning sodium alginate hydrogels with sustained submucosal lift for endoscopic submucosal dissection. *Int. J. Biol. Macromol.* **2022**, *223*, 939−949.

(18) Lei, X. X.; Hu, J. J.; Zou, C. Y.; Jiang, Y. L.; Zhao, L. M.; Zhang, X. Z.; Li, Y. X.; Peng, A. N.; Song, Y. T.; Huang, L. P.; Li-Ling, J.; Xie, H. Q. Multifunctional two-component in-situ hydrogel for esophageal submucosal dissection for mucosa uplift, postoperative wound closure and rapid healing. *Bioact. Mater.* **2023**, *27*, 461−473.

(19) Dave, H.; Vithalani, H.; Singh, H.; Yadav, I.; Jain, A.; Kumar, S.; Bhatia, Z.; Seshadri, S.; Hassan, S.; Dhanka, M. Easily injectable gelatin-nonanal hydrogel for endoscopic resectioning of gastrointestinal polyps. *Int. J. Biol. Macromol.* **2024**, *279*, 135405.

(20) Liu, Y.; Lang, C.; Zhang, K.; Feng, L. L.; Li, J. Y.; Wang, T. T.; Sun, S. Y.; Sun, G. W. Injectable chitosan-polyvinylpyrrolidone composite thermosensitive hydrogels with sustained submucosal lifting for endoscopic submucosal dissection. *Int. J. Biol. Macromol.* **2024**, *276*, 133165.

(21) Fan, C. Q.; Xu, K. G.; Huang, Y.; Liu, S.; Wang, T. C.; Wang, W.; Hu, W. C.; Liu, L.; Xing, M.; Yang, S. M. Viscosity and degradation controlled injectable hydrogel for esophageal endoscopic submucosal dissection. *Bioact. Mater.* **2021**, *6*, 1150−1162.

(22) Cui, S. Q.; Wei, Y. M.; Bian, Q.; Zhu, Y.; Chen, X. B.; Zhuang, Y. P.; Cai, M. Y.; Tang, J. Y.; Yu, L.; Ding, J. D. Injectable Thermogel Generated by the "Block Blend" Strategy as a Biomaterial for Endoscopic Submucosal Dissection. *ACS Appl. Mater. Interfaces* **2021**, *13*, 19778−19792.

(23) Ni, P.; Ye, S.; Li, R.; Shan, J.; Yuan, T.; Liang, J.; Fan, Y.; Zhang, X. Chitosan thermosensitive hydrogels based on lyophilize powders demonstrate significant potential for clinical use in endoscopic submucosal dissection procedures. *Int. J. Biol. Macromol.* **2021**, *184*, 593−603.

(24) Ni, P. X. Z.; Li, R. P.; Ye, S.; Shan, J.; Yuan, T.; Liang, J.; Fan, Y. J.; Zhang, X. D. Lactobionic acid-modified chitosan thermosensitive hydrogels that lift lesions and promote repair in endoscopic submucosal dissection. *Carbohydr. Polym.* **2021**, *263*, 118001.

(25) Liu, S. R.; Ju, R. B.; Zhang, Z. G.; Jiang, Z.; Cui, J. Z.; Liu, W. S.; Han, B. Q.; Wang, S. Temperature-sensitive injectable chitosan-based hydrogel for endoscopic submucosal dissection. *Int. J. Biol. Macromol.* **2024**, *282*, 136566.

(26) Zhang, Y.; Miao, D. T.; Su, M. L.; Tang, Y. X.; Zhou, M. H.; Yu, Y.; Guo, X. F.; Wu, D. C. Synergistic Drug-Loaded Shear-Thinning Star Polymer Hydrogel Facilitates Gastrointestinal Lesion

Resection and Promotes Wound Healing. *Adv. Sci.* **2024**, *11*, 2309586.

(27) Wang, P. H.; Li, R. X.; Ma, J. P.; Zhang, W. J.; Shen, H. F.; Ren, Y. H.; Zhang, X.; Li, S.; Chi, B. Facilitating safe and sustained submucosal lift through an endoscopically injectable shear-thinning carboxymethyl starch sodium hydrogel. *Carbohydr. Polym.* **2024**, *336*, 122128.

(28) Pang, Y.; Liu, J.; Moussa, Z. L.; Collins, J. E.; Mcdonnell, S.; Hayward, A. M.; Jajoo, K.; Langer, R.; Traverso, G. Endoscopically Injectable Shear-Thinning Hydrogels Facilitating Polyp Removal. *Adv. Sci.* **2019**, *6*, 1901041.

(29) Chen, X.; Nishiguchi, A.; Taguchi, T. Adhesive Submucosal Injection Material Based on the Nonanal Group-Modified Poly(vinyl alcohol)/α-Cyclodextrin Inclusion Complex for Endoscopic Submucosal Dissection. *ACS Applied Bio Materials* **2020**, *3*, 4370−4379.

(30) Cho, R. A.; Kamata, H.; Tsuji, Y.; Fujisawa, A.; Miura, Y.; Ishikawa, S.; Sato, R.; Katashima, T.; Sakai, T.; Fujishiro, M. Optimizing a self-solidifying hydrogel as an endoscopically deliverable hydrogel coating system: a proof-of-concept study on porcine endoscopic submucosal dissection-induced ulcers. *Polym. J.* **2024**, *56*, 855−863.

(31) Zhang, X.; He, Y.; Li, X.; Lin, C. C.; Yuan, Z.; Dai, L. L.; Ma, F.; Lv, Y.; Huang, T. J.; Ren, M. D.; Cai, K. Y.; He, S. X. Biocompatible, adhesive and stable GelMAc/PVAMA/MPDA@Cur hydrogels regulate immune response to improve endoscopic submucosal dissection-induced gastric ulcer healing in vivo. *Appl. Mater. Today* **2022**, *28*, 101539.

(32) Feng, W. J.; Wu, Y. H.; Liu, X. Y.; Wang, Z. K. Shear-thinning Catechol-modified Chitosan Hydrogel Loaded with Silver Nanoparticles for Endoscopic Submucosal Dissection. *Chin. J. Polym. Sci.* **2024**, *42*, 1147−1155.

(33) Rodriguez, E. A.; Tran, G. N.; Gross, L. A.; Crisp, J. L.; Shu, X.; Lin, J. Y.; Tsien, R. Y. A far-red fluorescent protein evolved from a cyanobacterial phycobiliprotein. *Nat. Methods* **2016**, *13*, 763−769.

(34) Lian, Y. Z.; Lin, I. H.; Yang, Y.-C.; Chao, J. C. J. Gastroprotective effect of Lycium barbarum polysaccharides and C-phycocyanin in rats with ethanol-induced gastric ulcer. *Int. J. Biol. Macromol.* **2020**, *165*, 1519−1528.

(35) Romay, C.; Armesto, J.; Remirez, D.; González, R.; Ledon, N.; García, I. Antioxidant and anti-inflammatory properties of C-phycocyanin from blue-green algae. *Inflammation Res.* **1998**, *47*, 36−41.

(36) Alzokaky, A. . a.-M.; Abdelkader, E. M.; El-Dessouki, A. M.; Khaleel, S. A.; Raslan, N. A. C-phycocyanin protects against ethanol-induced gastric ulcers in rats: Role of HMGB1/NLRP3/NF-κB pathway. *Basic Clin. Pharmacol. Toxicol.* **2020**, *127*, 265−277.

(37) Wu, B.; Cheng, H.; Li, X.; Yang, Q.; Zhang, W.; Hao, S.; Wang, C. Phycocyanin-derived bioactive peptide PCP3 ameliorates lipopolysaccharide-induced small intestinal inflammation in murine intestinal organoids and mice through regulating Akt and AMPK/autophagy signaling. *Food Bioscience* **2024**, *60*, 104419.

(38) Dev, A.; Mohanbhai, S. J.; Kushwaha, A. C.; Sood, A.; Sardoiwala, M. N.; Choudhury, S. R.; Karmakar, S. κ-carrageenan-C-phycocyanin based smart injectable hydrogels for accelerated wound recovery and real-time monitoring. *Acta Biomater.* **2020**, *109*, 121−131.

(39) Li, Z.; Qian, C.; Zheng, X.; Qi, X.; Bi, J.; Wang, H.; Cao, J. Collagen/chitosan/genipin hydrogel loaded with phycocyanin nanoparticles and ND-336 for diabetic wound healing. *Int. J. Biol. Macromol.* **2024**, *266*, 131220.

(40) Dong, J.; Lang, Y.; He, J.; Cui, J.; Liu, X.; Yuan, H.; Li, L.; Zhou, M.; Wang, S. Phycocyanin-based multifunctional microspheres for treatment of infected radiation-induced skin injury. *Biomaterials* **2025**, *317*, 123061.

(41) Liu, R.-Z.; Li, W.-J.; Zhang, J.-J.; Liu, Z.-Y.; Li, Y.; Liu, C.; Qin, S. The Inhibitory Effect of Phycocyanin Peptide on Pulmonary Fibrosis In Vitro. *Mar. Drugs* **2022**, *20*, 696.

(42) Oh, H. Y.; Choi, H. H.; Kim, E. J.; Choi, J. H.; Choi, S. S.; Lee, H. K.; Kim, H. K.; Kim, S. W.; Park, W. S. H.; Chae, H. S. In vitro and in vivo phototoxicity on gastric mucosa induced by methylene blue. *Saudi J. Gastroenterol.* **2023**, *29*, 53−58.

(43) Olliver, J. R.; Wild, C. P.; Sahay, P.; Dexter, S.; Hardie, L. J. Chromoendoscopy with methylene blue and associated DNA damage in Barrett's oesophagus. *Lancet* **2003**, *362*, 373−374.

(44) Wang, H.; Chen, X.; Wen, Y.; Li, D.; Sun, X.; Liu, Z.; Yan, H.; Lin, Q. A Study on the Correlation between the Oxidation Degree of Oxidized Sodium Alginate on Its Degradability and Gelation. *Polymers* **2022**, *14*, 1679.

(45) Raina, N.; Pahwa, R.; Thakur, V. K.; Gupta, M. Polysaccharide-based hydrogels: New insights and futuristic prospects in wound healing. *Int. J. Biol. Macromol.* **2022**, *223*, 1586−1603.

(46) Zhao, L.; Feng, Z.; Lyu, Y.; Yang, J.; Lin, L.; Bai, H.; Li, Y.; Feng, Y.; Chen, Y. Electroactive injectable hydrogel based on oxidized sodium alginate and carboxymethyl chitosan for wound healing. *Int. J. Biol. Macromol.* **2023**, *230*, 123231.

(47) Zhang, W.; Geng, X.; Qin, S.; Xie, Z.; Li, W.; Li, J. Research progress and application of chitosan dressings in hemostasis: A review. *Int. J. Biol. Macromol.* **2024**, *282*, 136421.

(48) Zhuxin, L.; Biao, Y.; Badamkhand, D.; Yifan, C.; Honghong, S.; Xiao, X.; Mingqian, T.; Zhixiang, W.; Chongjiang, C. Carboxylated chitosan improved the stability of phycocyanin under acidified conditions. *Int. J. Biol. Macromol.* **2023**, *233*, 123474.

(49) Zhang, L.; Li, Q.; Bai, X.; Li, X.; Zhang, G.; Zou, J.; Fei, P.; Lai, W. Double network self-healing hydrogels based on carboxyethyl chitosan/oxidized sodium alginate/Ca2+: Preparation, characterization and application in dye absorption. *Int. J. Biol. Macromol.* **2024**, *264*, 130564.

(50) Cassano, R.; Perri, P.; Scarcello, E.; Piro, P.; Sole, R.; Curcio, F.; Trombino, S. Chitosan Hemostatic Dressings: Properties and Surgical Applications. *Polymers* **2024**, *16*, 1770.

(51) Ms, M.; Venkatasubbu, G. D. Modulating Coagulation via Bioinspired Mesoporous Calcium-Decorated Silica Nanoparticles for Efficient Fibrin Clot Formation. *ACS Applied Bio Materials* **2024**, *7*, 6998−7008.

(52) Sousa, A. B.; Águas, A. P.; Barbosa, M. A.; Barbosa, J. N. Immunomodulatory biomaterial-based wound dressings advance the healing of chronic wounds via regulating macrophage behavior. *Regen. Biomater.* **2022**, *9*, rbac065.

(53) Mao, J.; Chen, L.; Cai, Z.; Qian, S.; Liu, Z.; Zhao, B.; Zhang, Y.; Sun, X.; Cui, W. Advanced Biomaterials for Regulating Polarization of Macrophages in Wound Healing. *Adv. Funct. Mater.* **2022**, *32*, 2111003.

(54) Hsieh-Lo, M.; Castillo, G.; Ochoa-Becerra, M. A.; Mojica, L. Phycocyanin and phycoerythrin: Strategies to improve production yield and chemical stability. *Algal Res.* **2019**, *42*, 101600.

(55) Wang, L.; Lu, Q.; Gao, W.; Yu, S. Recent advancement on development of drug-induced macrophage polarization in control of human diseases. *Life Sci.* **2021**, *284*, 119914.

(56) Hao, S.; Yan, Y.; Huang, W.; Gai, F.; Wang, J.; Liu, L.; Wang, C. C.-. C-phycocyanin reduces inflammation by inhibiting NF-κB activity through downregulating PDCD5 in lipopolysaccharide-induced RAW 264.7 macrophages. *J. Funct. Foods.* **2018**, *42*, 21−29.

(57) Zhu, C.; Ling, Q.; Cai, Z.; Wang, Y.; Zhang, Y.; Hoffmann, P. R.; Zheng, W.; Zhou, T.; Huang, Z. Selenium-Containing Phycocyanin from Se-Enriched Spirulina platensis Reduces Inflammation in Dextran Sulfate Sodium-Induced Colitis by Inhibiting NF-κB Activation. *J. Agric. Food Chem.* **2016**, *64*, 5060−5070.

(58) Liu, R.; Qin, S.; Li, W. Phycocyanin: Anti-inflammatory effect and mechanism. *Biomed. Pharmacother.* **2022**, *153*, 113362.

(59) Liu, Q.; Li, W.; Qin, S. Therapeutic effect of phycocyanin on acute liver oxidative damage caused by X-ray. *Biomed. Pharmacother.* **2020**, *130*, 110553.

(60) Kim, K. M.; Lee, J. Y.; Im, A.-R.; Chae, S. Phycocyanin Protects Against UVB-induced Apoptosis Through the PKC α/βII-Nrf-2/HO-1 Dependent Pathway in Human Primary Skin Cells. *Molecules* **2018**, *23*, 478.

(61) Gao, Y.; Liu, C.; Wan, G.; Wang, X.; Cheng, X.; Ou, Y. Phycocyanin prevents methylglyoxal-induced mitochondrial-dependent apoptosis in INS-1 cells by Nrf2. *Food Funct.* **2016**, *7*, 1129−1137.

(62) Mahendra, J.; Mahendra, L.; Muthu, J.; John, L.; Romanos, G. E. Clinical Effects of Subgingivally Delivered Spirulina Gel in Chronic Periodontitis Cases: A Placebo Controlled Clinical Trial. *J. Clin. Diagn. Res.* **2013**, *7*, 2330−2333.

(63) Patil, S.; Al-Zarea, B. K.; Maheshwari, S.; Sahu, R. Comparative evaluation of natural antioxidants spirulina and aloe vera for the treatment of oral submucous fibrosis. *J. Oral Biol. Craniofac. Res.* **2015**, *5*, 11−15.

(64) Jalali, P.; Almasi, P.; Faramarzi, M.; Hamishehkar, H.; Kouhsoltani, M. Effect of spirulina platensis algae purified bioactive peptides on wound healing after periodontal flap surgery: a randomized clinical trial. *Sci. Rep.* **2025**, *15*, 17971.

(65) Manzon-Reyes, L. V. L. A.; Andaya, A. G. The effects of Spirulina (Arthrospira platensis) dietary supplement as an adjunct therapy for children aged 7−14 years old with asthma: A randomized − double blind placebo controlled clinical trial. *J. Allergy Clin. Immunol.* **2018**, *141*, AB208.

(66) Tamtaji, O. R.; Heidari-Soureshjani, R.; Asemi, Z.; Kouchaki, E. The effects of spirulina intake on clinical and metabolic parameters in Alzheimer's disease: A randomized, double-blind, controlled trial. *Phytother. Res.* **2023**, *37*, 2957−2964.

(67) Ghaem Far, Z.; Babajafari, S.; Kojuri, J.; Mohammadi, S.; Nouri, M.; Rostamizadeh, P.; Rahmani, M. H.; Azadian, M.; Ashrafi-Dehkordi, E.; Zareifard, A.; Golchin Vafa, R.; Mazloomi, S. M. Antihypertensive and antihyperlipemic of spirulina (Arthrospira platensis) sauce on patients with hypertension: A randomized triple-blind placebo-controlled clinical trial. *Phytother. Res.* **2021**, *35*, 6181−6190.